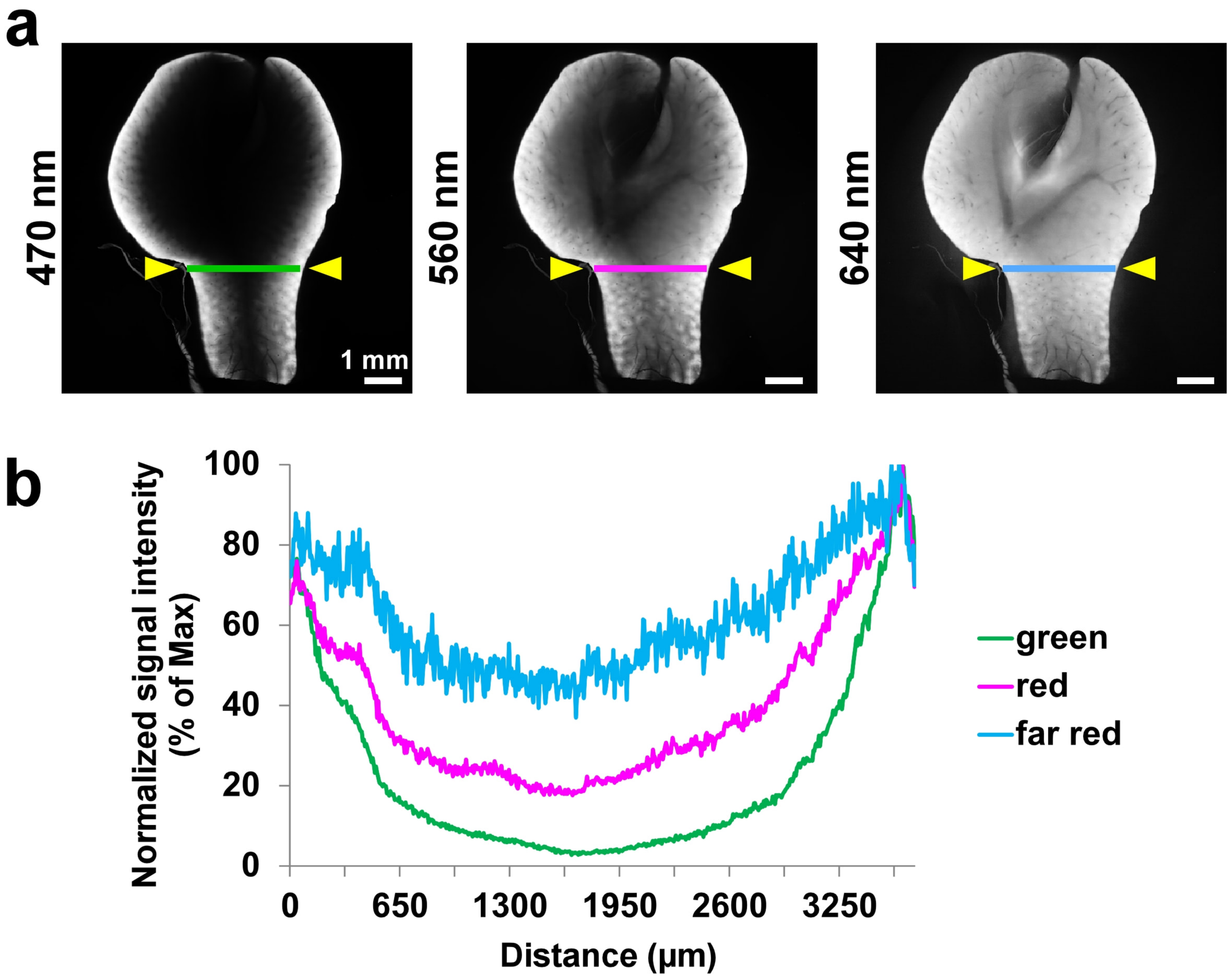

Supplementary Figure 1

Light penetration deep in tissue at different wavelengths

(**a**) Demonstration of tissue penetration of the light at different imaging wavelengths. The same liver region (without any labeling) of a cleared mouse imaged in green (ex: 470 nm) (left), red (ex: 560 nm) (middle) and far-red channels (ex: 640 nm) (right) using light-sheet microscopy. (**b**) Fluorescence signal intensity profiles normalized over the maximum intensity of the regions indicated by the lines in a. Complete illumination of cleared liver at 640 nm compared to other wavelengths is evident. Similar results were observed in 10 independent animals.

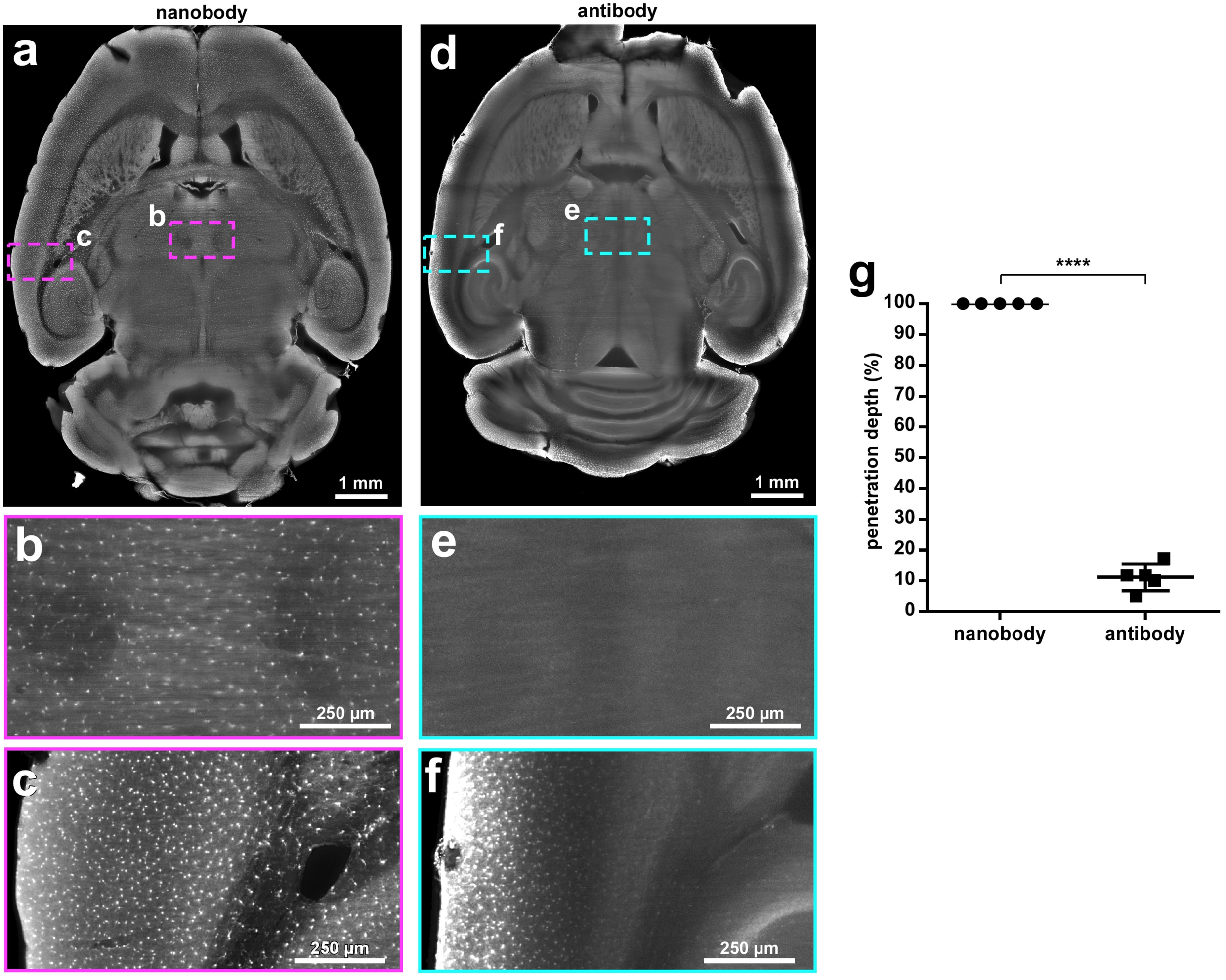

Supplementary Figure 2

Deep tissue staining efficiency of nanobody vs conventional antibody

Penetration depth comparison between anti-GFP nanobody (**a**-**c**) vs. conventional anti-GFP antibody (**d**-**f**) from brains coming from CX3CR1$^{GFP/+}$ mice. Representative images of 1 brain from each group consisting of 5 independent animals. (**g**) Penetration depth quantifications of anti-GFP nanobody vs. conventional anti-GFP antibody stained brains from 5-12 months old CX3CR1$^{GFP/+}$ mice (mean ± s.d.; n=5 mice per group; statistical significance (****$p < 0.0001$) was assessed by two tailed *t*-test)

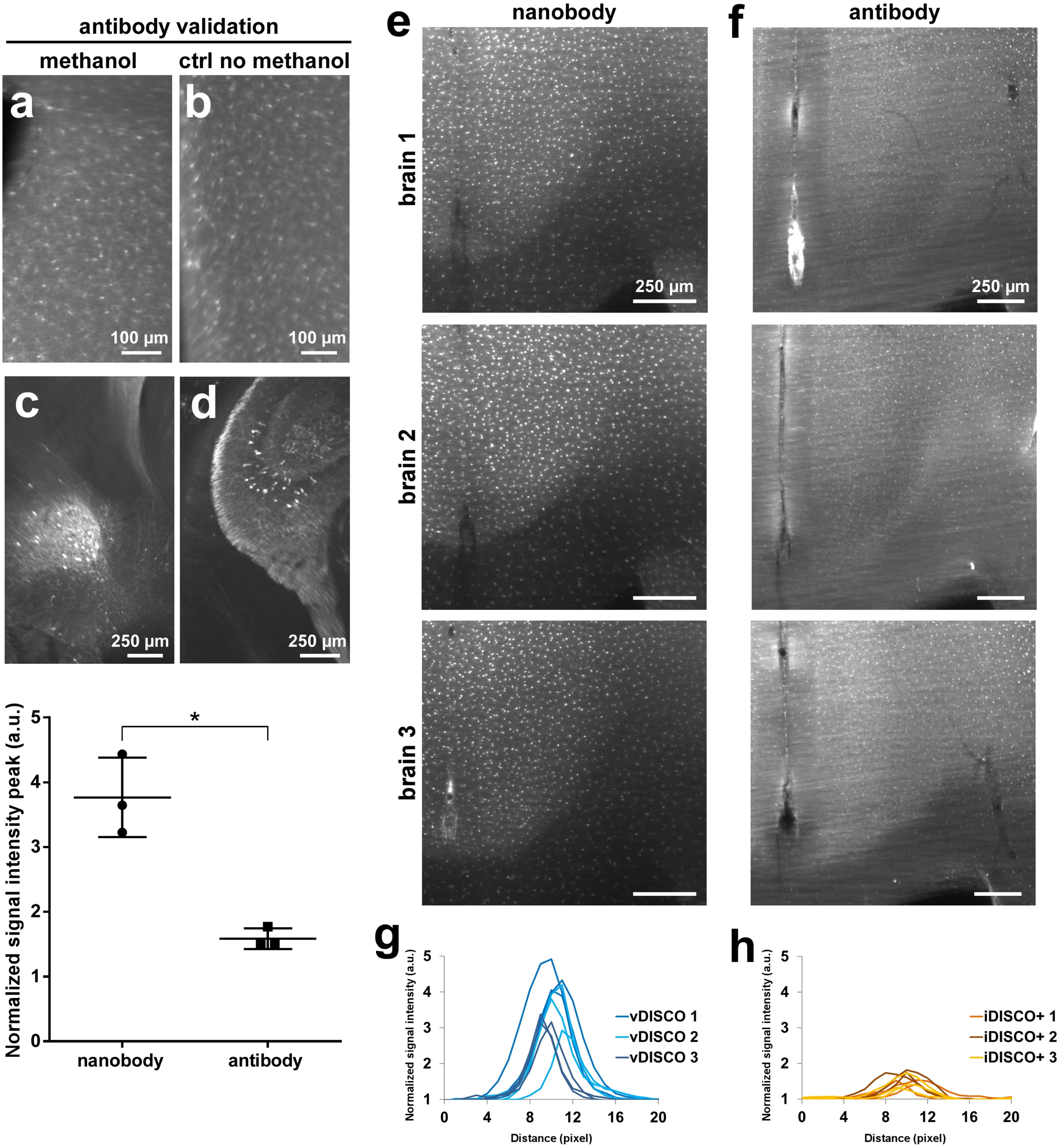

Supplementary Figure 3

Compatibility test of conventional anti-GFP antibody with iDISCO+ protocol and comparison between vDISCO passive boosting with anti-GFP nanobooster vs iDISCO+ passive labeling with conventional anti-GFP antibody on CX3CR1$^{GFP/+}$ brains

(**a**-**d**) Fluorescent stereomicroscope images of 600 µm brain slices from CX3CR1$^{GFP/+}$ animal (**a**,**b**), and GFPM animal (both 2-3 months old) (**c**,**d**) showing the compatibility of a conventional anti-GFP antibody with methanol pretreatment: (**a**) slice from CX3CR1$^{GFP/+}$ brain and (**c**) slice from GFPM brain both pretreated with methanol and labeled with the conventional anti-GFP antibody showing the persistence of fluorescence signal compared with: (**b**) slice from the same CX3CR1 brain and (**d**) slice from the same GFPM brain labeled with the conventional anti-GFP antibody without methanol pretreatment as positive control. Similar results were observed in 2 independent animals. (**e**-**i**) Comparison between passive vDISCO boosting with anti-GFP nanobooster (conjugated with Atto-647N) vs. passive iDISCO+ labeling with the tested conventional anti-GFP antibody (conjugated with Alexa-647) on CX3CR1$^{GFP/+}$ whole brains from 5-7 months old mice: (**e**,**f**) light-sheet images showing the difference in labeling after vDISCO (**e**) vs. iDISCO+ (**f**) at the level of the same anatomical region (cortex and corpus callosum) in 3 different independent brains per each group; (**g**,**h**) plots of signal intensity profiles from vDISCO boosted brains in e (**g**) and iDISCO+ labeled brains in f (**h**); (**i**) Comparison of the peaks of the signal intensity profiles in g vs. h (mean ± s.d., n=3 animals per group, statistical significance (*p = 0.02) was assessed by two tailed t-test).

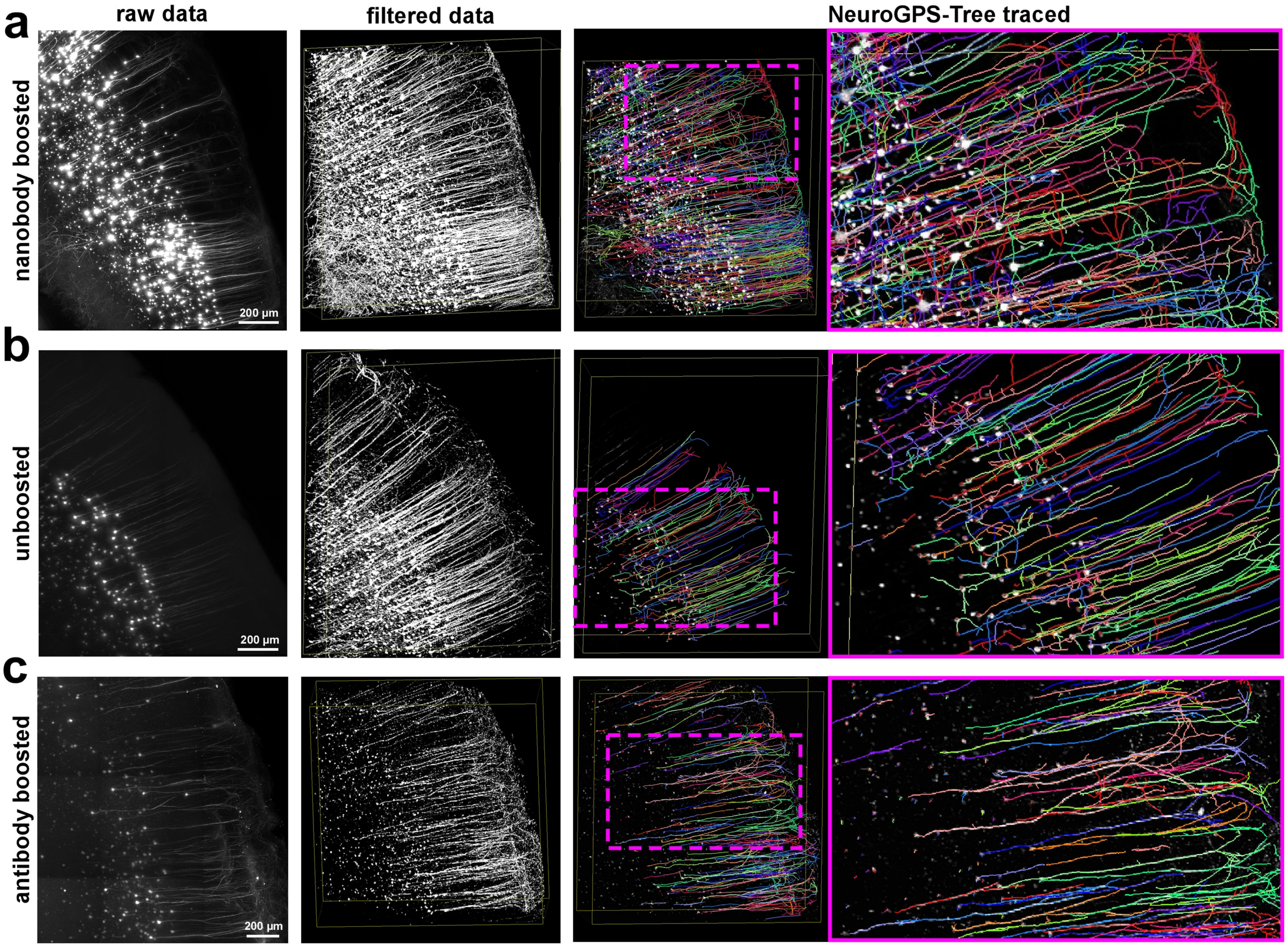

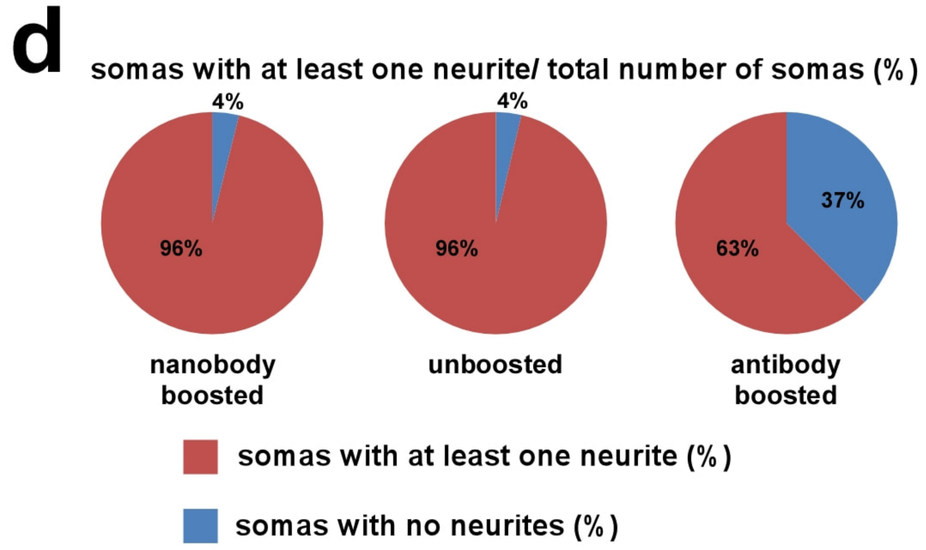

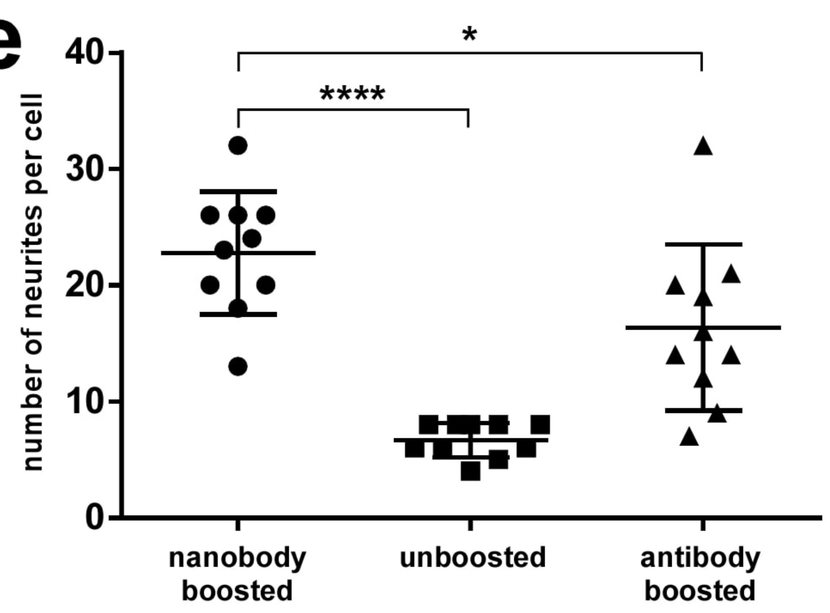

Supplementary Figure 4

Neuron tracing with NeuroGPS-Tree

(**a**-**c**) Tracing of neurons in vDISCO nanobody boosted (**a**), unboosted (**b**) and iDISCO+ conventional anti-GFP antibody boosted (**c**) brains from 6-13 weeks old *Thy1*-GFPM mice using NeuroGPS-Tree algorithms. The scans were obtained with a commercial light-sheet microscope (Ultramicroscope II, LaVision Biotec), optimized for large cleared tissue imaging, thereby with lower resolution compared to standard confocal microscopes. From left to right: raw image, equalized & filtered images, and NeuroGPS-Tree traced neuronal structures are shown: all the neurites belonging to a neuron are represented by the same color. Neuronal soma identified by NeuroGPS-Tree are represented by red dots. Single experiment per each method. (**d**) Quantification of number of detected neurons characterized by their soma with at least one detected neurite over the total number of detected somas in vDISCO boosted vs unboosted and conventional antibody boosted samples. While in vDISCO boosted and unboosted cases almost all the neurons were detected with at least one neurite per soma, in the antibody boosted case only 63% was detected with neurites (**e**) Quantification of number of detected neurites per neuron in vDISCO boosted vs. unboosted and conventional antibody boosted samples, showing that only vDISCO allows the tracing of more neurites per cell (mean ± s.d; n=10 neurons per group; statistical significance ($F_{2,27}$=24.30, ****p < 0.0001,*p = 0.02) was assessed by one-way ANOVA followed by Dunnett´s *post hoc* test).

raw data

filtered data

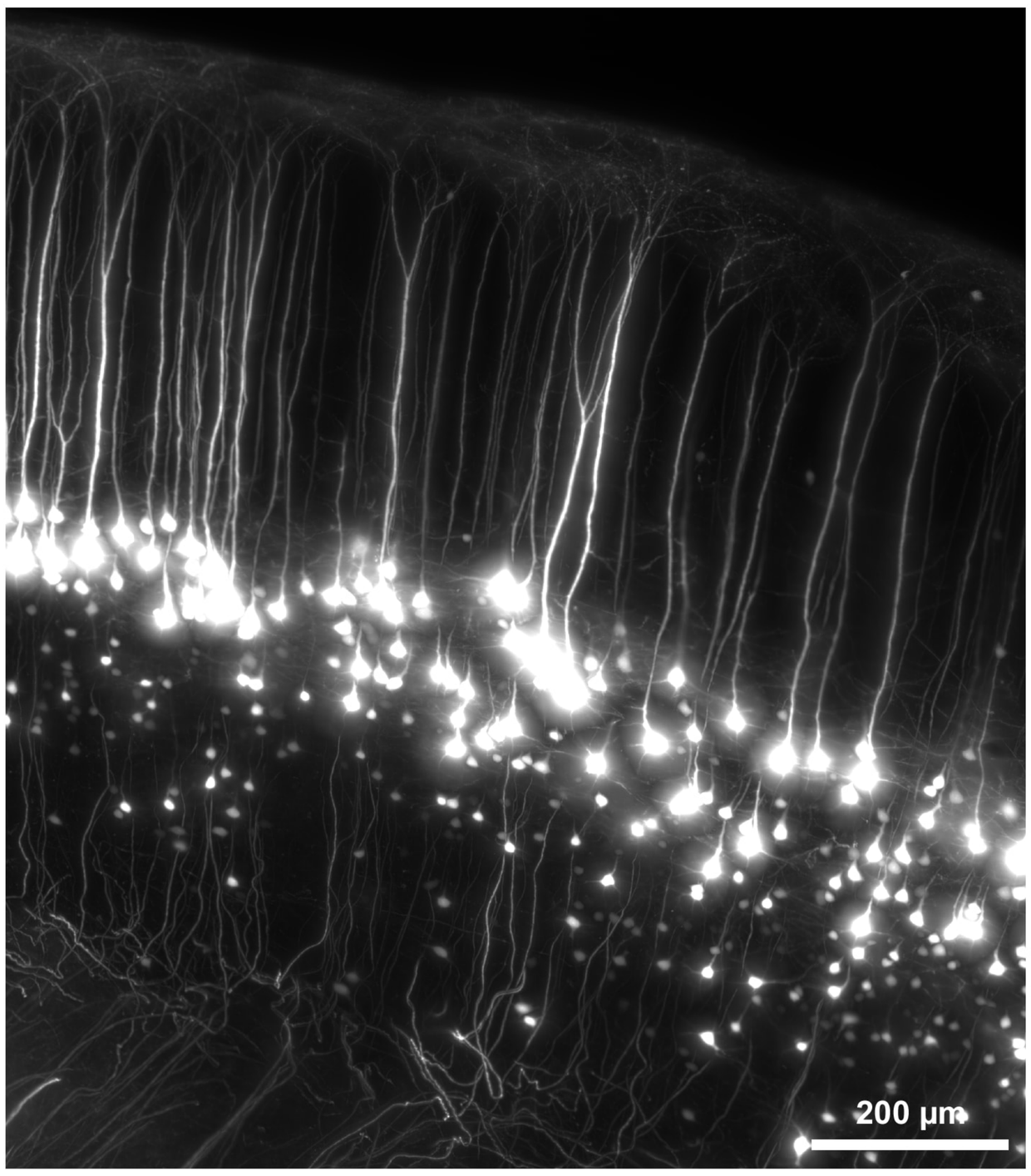

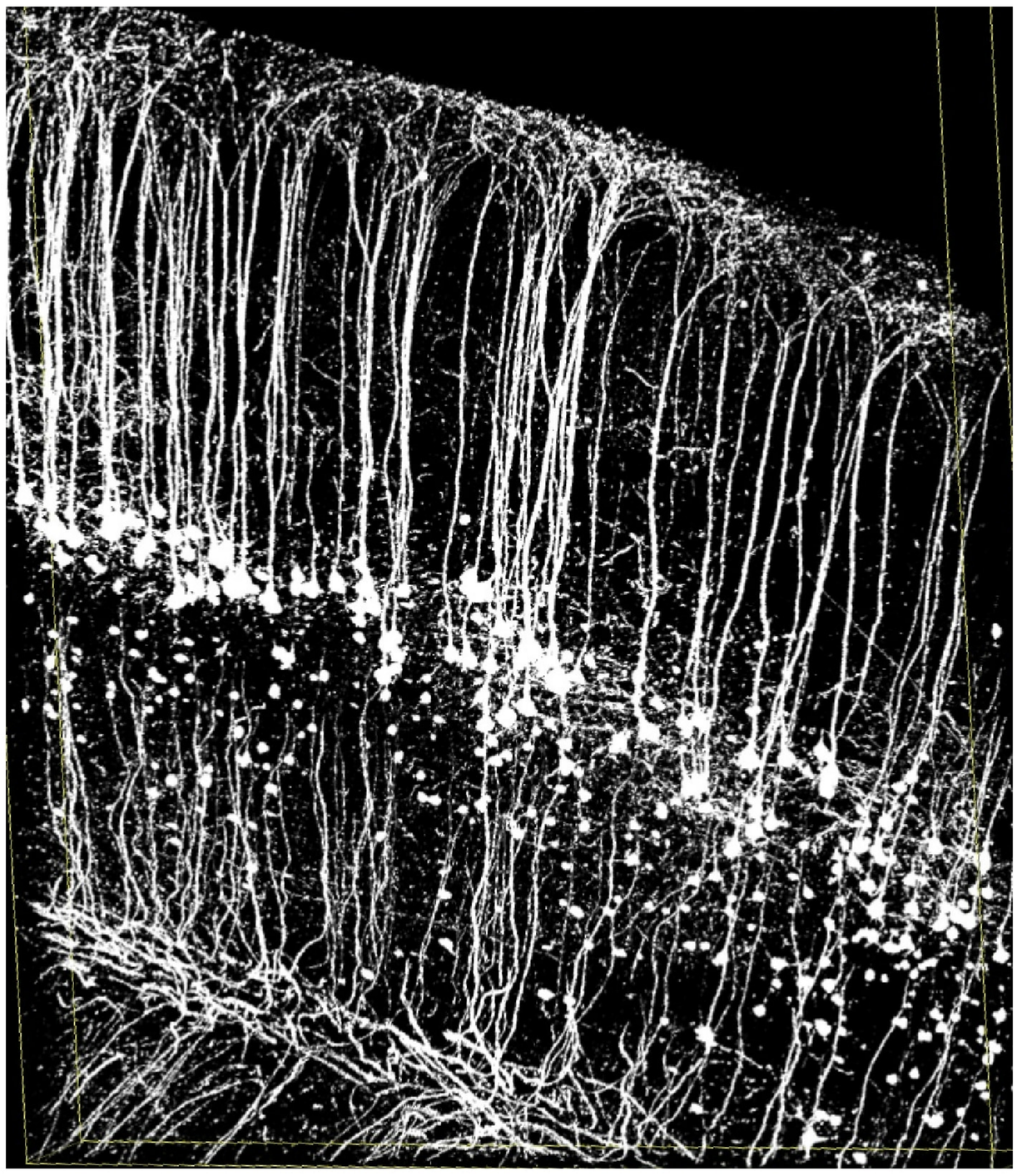

NeuroGPS-Tree traced

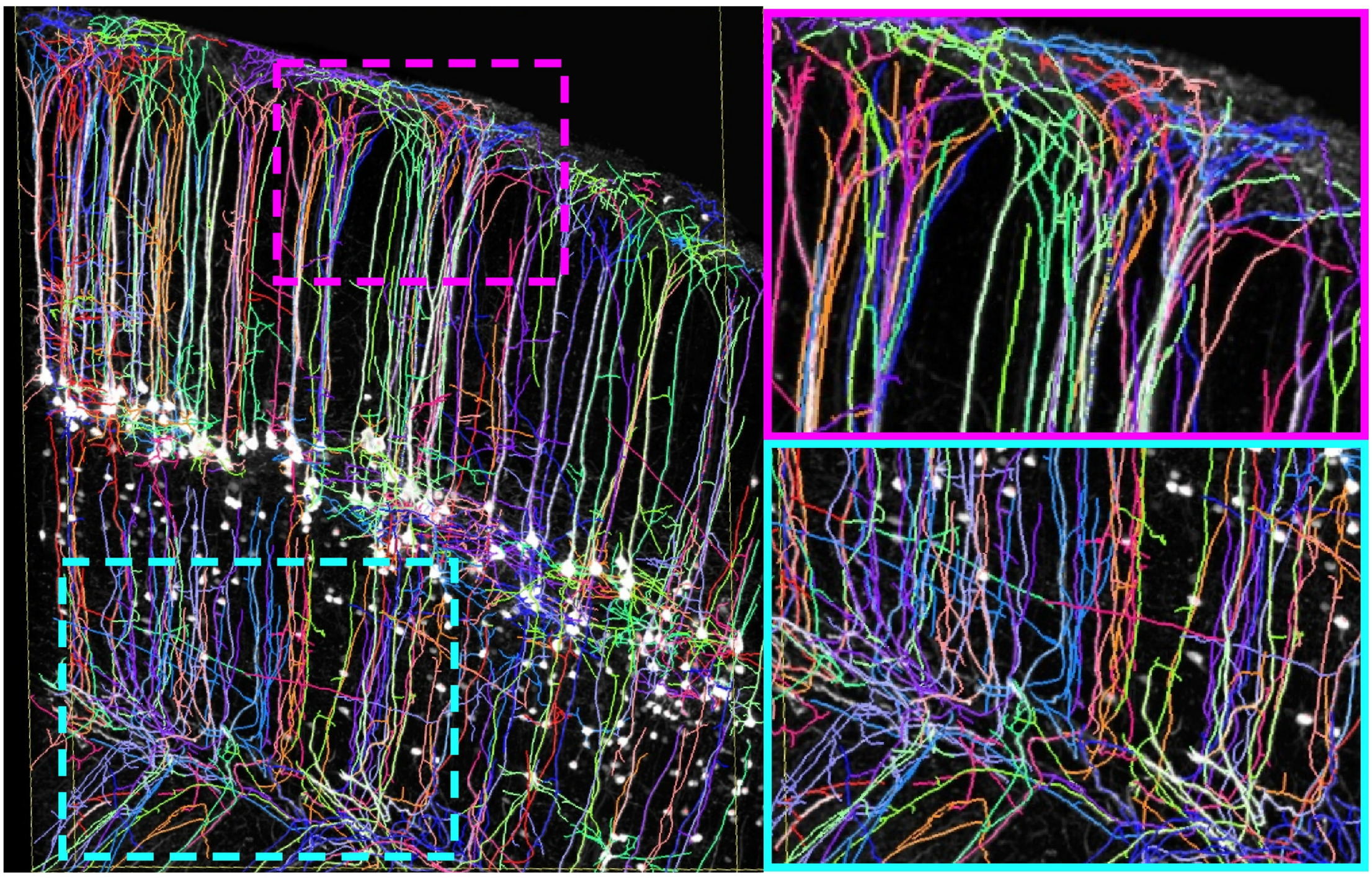

Supplementary Figure 5

Neuron tracing with NeuroGPS-Tree, secondary somatosensory cortex

Tracing of neurons in vDISCO boosted brain from a 6 weeks old *Thy1*-GFPM mouse using NeuroGPS-Tree algorithms. The displayed region is around the secondary somatosensory cortex (Region S2 of the Figure 152 of the Franklin & Paxinos atlas, Bregma -2.80, Interaural 3.00). The scans were obtained with a commercial light-sheet microscope (Ultramicroscope II, LaVision Biotec), optimized for large cleared tissue imaging, thereby with lower resolution compared to standard confocal microscopes. From left, right to down: raw image, equalized & filtered images, and NeuroGPS-Tree traced neuronal structures are shown: all the neurites belonging to a neuron are represented by the same color. Axons projecting out from the somas to the corpus callosum are visible and traced. Single experiment.

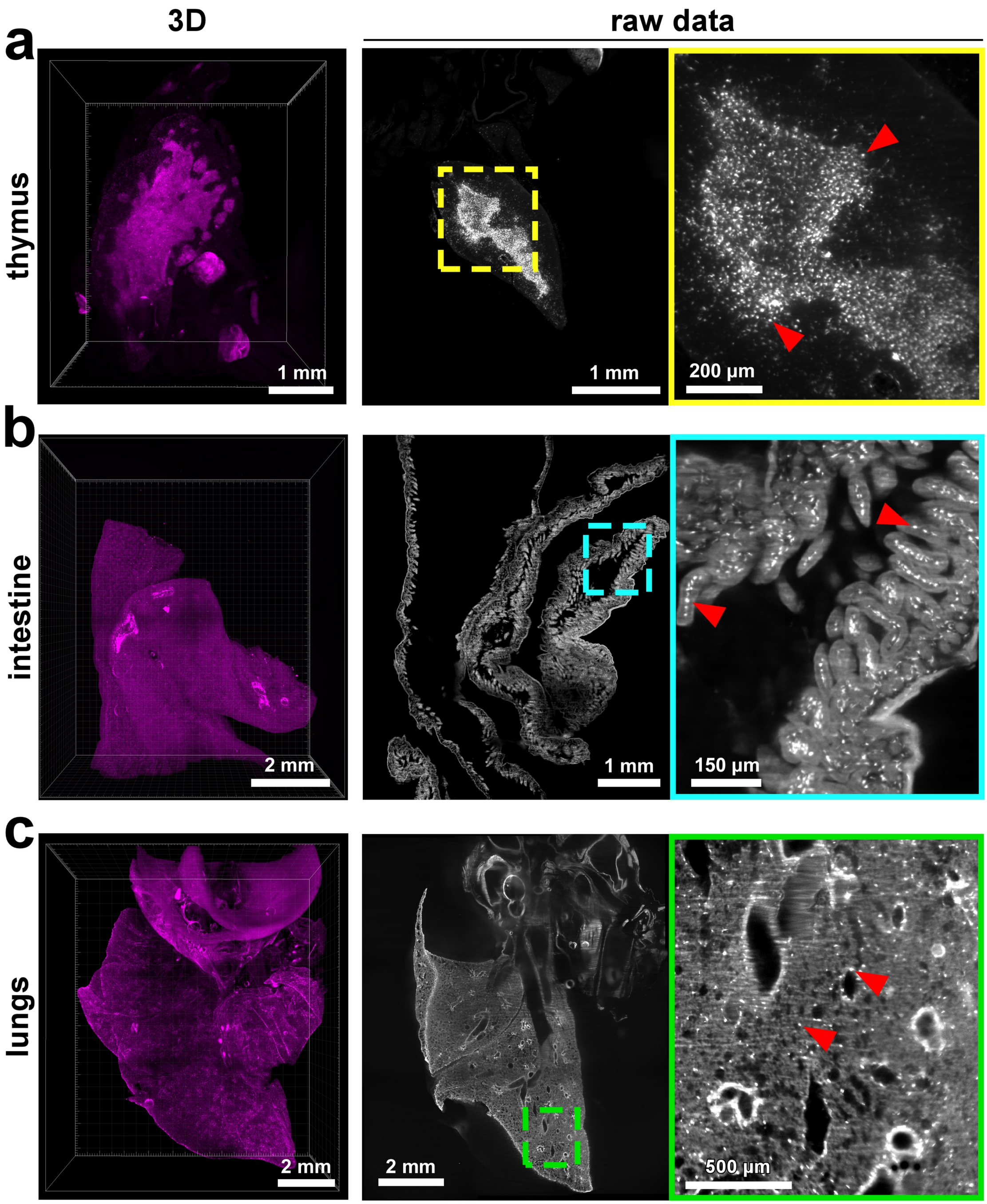

Supplementary Figure 6

Visualization of CX3CR1 GFP+ cells in individual organs

(**a**-**c**) 3D visualization (magenta) and raw data images (grey) of individual organs including thymus (**a**), intestine (**b**), and lungs (**c**) from a 6 months old CX3CR1$^{GFP/+}$ mouse imaged by light-sheet microscopy. Individual CX3CR1 GFP+ cells are indicated by red arrow-heads in the zoomed images from the boxed regions. Similar results were observed in 3 independent animals.

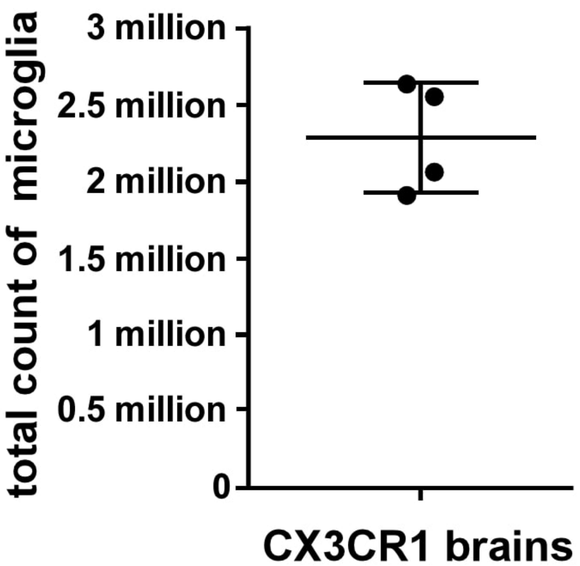

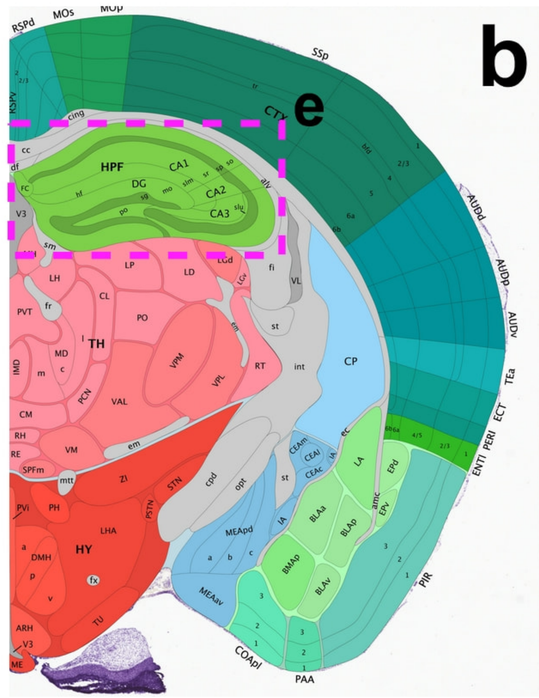

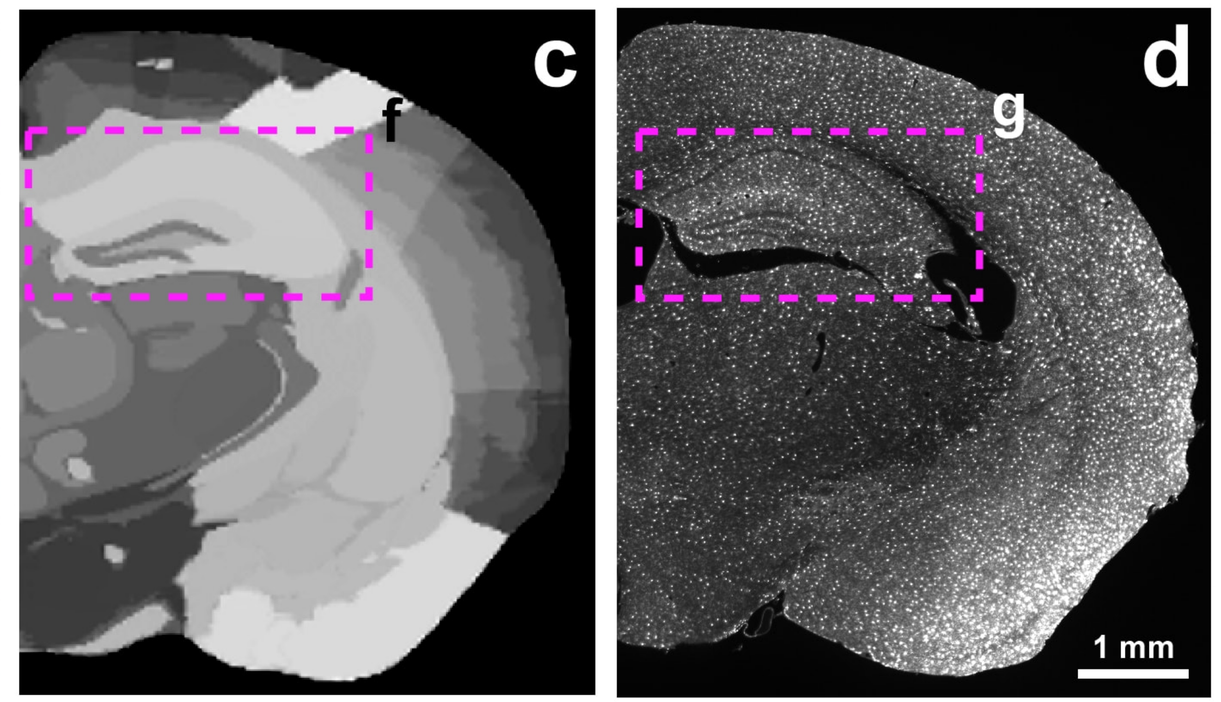

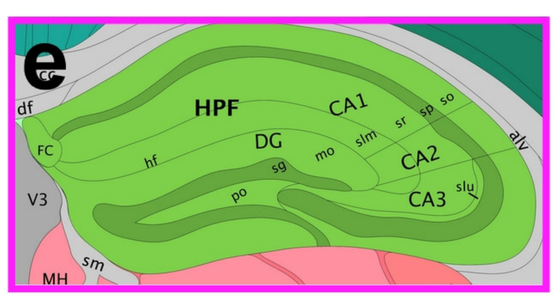

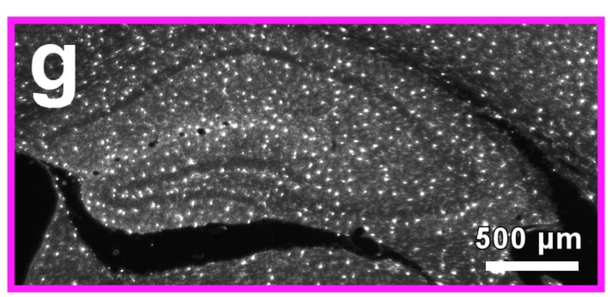

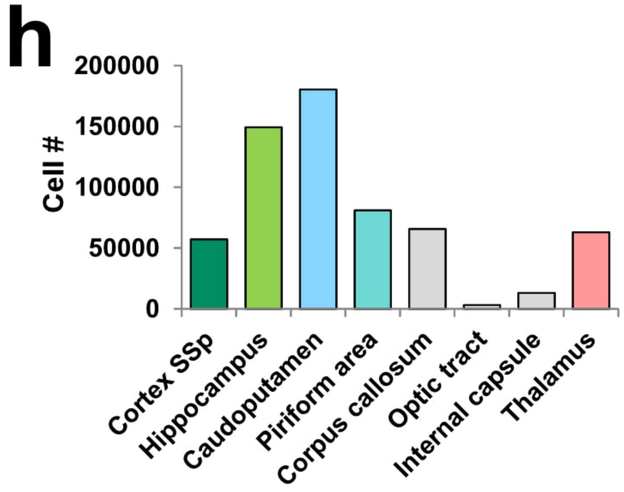

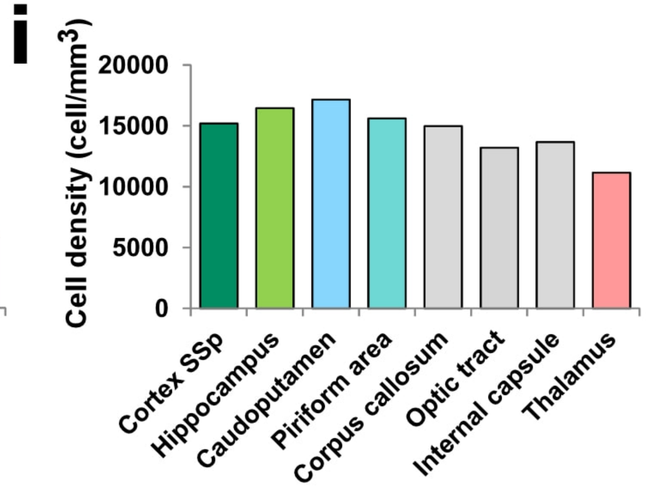

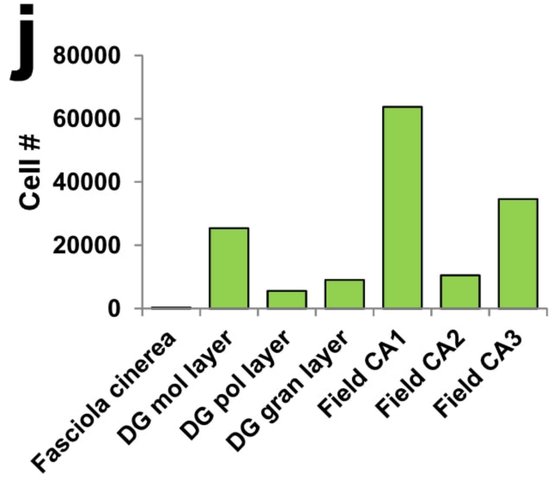

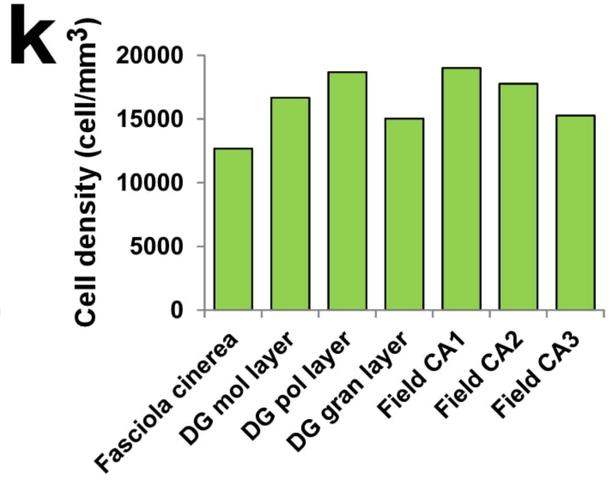

Supplementary Figure 7

Visualization and quantification of the signal from CX3CR1$^{GFP/+}$ mouse by vDISCO boosting

(**a**-**k**) Automated analysis of fluorescent cells quantification and distribution in CX3CR1$^{GFP/+}$ mouse brain after vDISCO boosting (mean ± s.d.; n = 4 2-5 months old mice: 2.647, 2.553, 1.909, 2.061 millions respectively (**a**)): (**b**) reference image from the Allen brain atlas, (**c**) registered reference annotation image, (**d**) the corresponding region in raw data in coronal view. (**e**-**g**) High magnification images of the region indicated in b-d containing the hippocampus. Automated quantification of absolute cell numbers (**h**) and cell densities (**i**) of the anatomical regions visible in b-d. Absolute cell numbers (**j**) and cell densities (**k**) of sub-regions of hippocampus shown in e-g. The quantifications include the cells in both brain hemispheres.

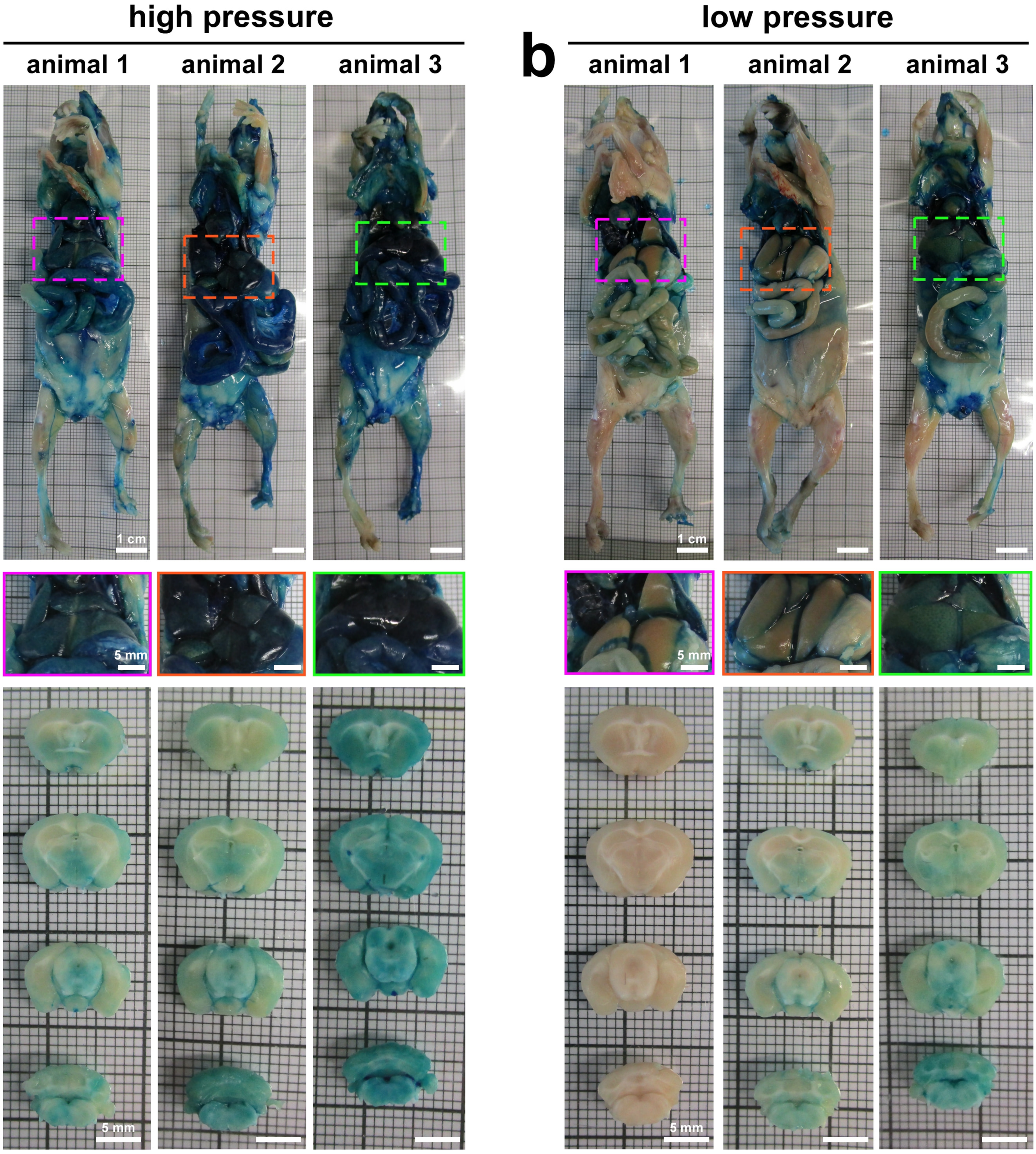

Supplementary Figure 8

Comparison between high vs low pressure transcardial perfusion
Diffusion of blue dye in the body (up) and brain (down) of 4 months old C57BL/6J animals trascardially perfused for 15 minutes with methylene blue with high pressure (approx. 180 mmHg) (**a**) vs low pressure (approx. 70 mmHg) (**b**). The colored rectangles (middle) show the high magnification images of the dashed regions at the level of the liver.

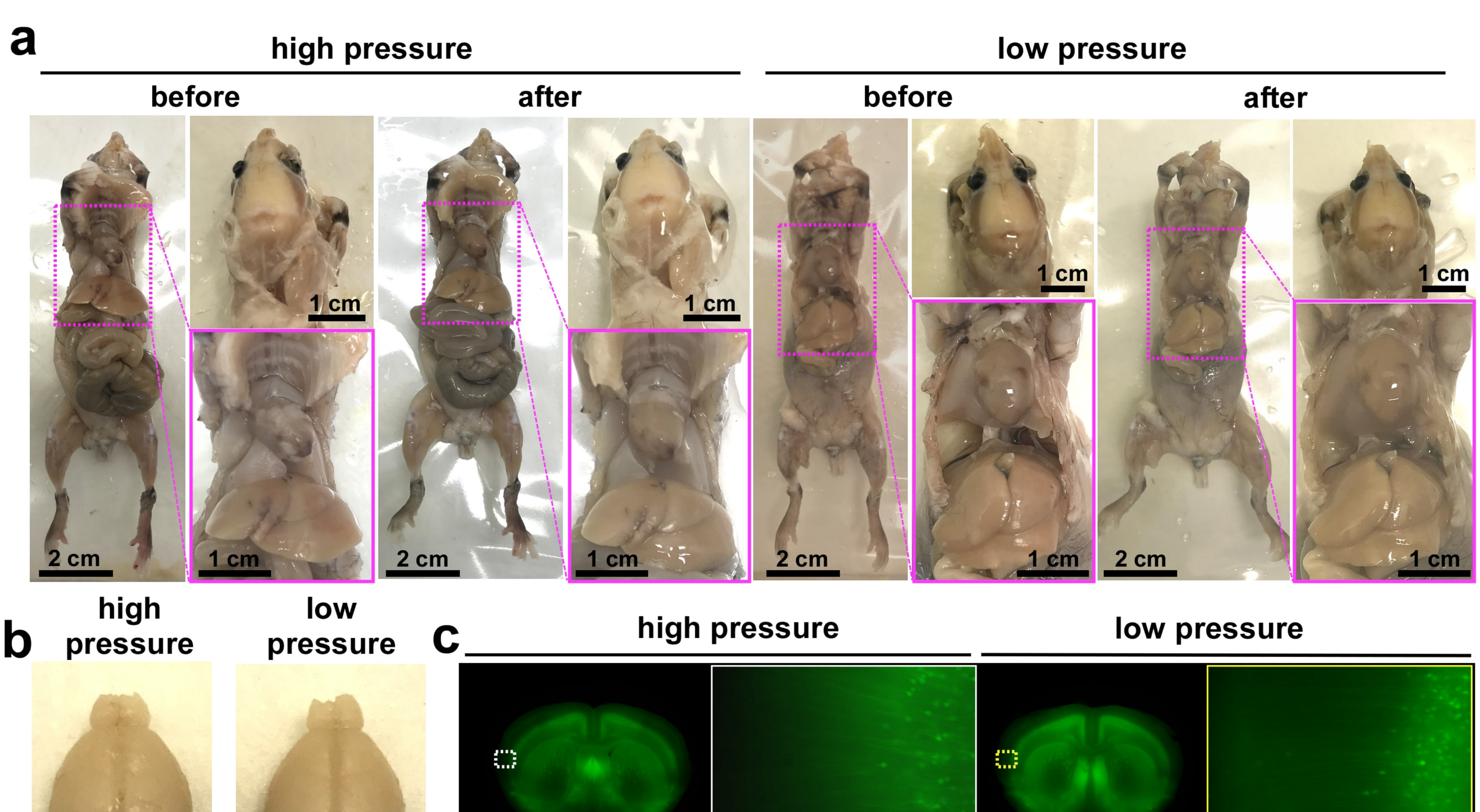

Supplementary Figure 9

Comparison between *Thy1*-YFPH line mice perfused with high (230 mmHg) or low pressure (110 mmHg)

(**a**) Images of 3 months old mice taken before and after high or low pressure perfusion for 3 days, showing no morphological organ changes due to high pressure perfusion. (**b**) Comparison of dissected brains and brain slices from mice after high or low pressure perfusion, showing that the brain was not deformed or disrupted by high pressure perfusion at the macroscopic scale (similar results were observed from 2 independent mice per group) (**c**) Using a stereo-fluorescent microscope, the cortical neurons were imaged at single cell resolution. No morphology changes in neuronal structures were detected at the microscopic scale indicating that the high (230 mmHg) pressure perfusion in the vDISCO protocol does not damage the tissue (single experiment).

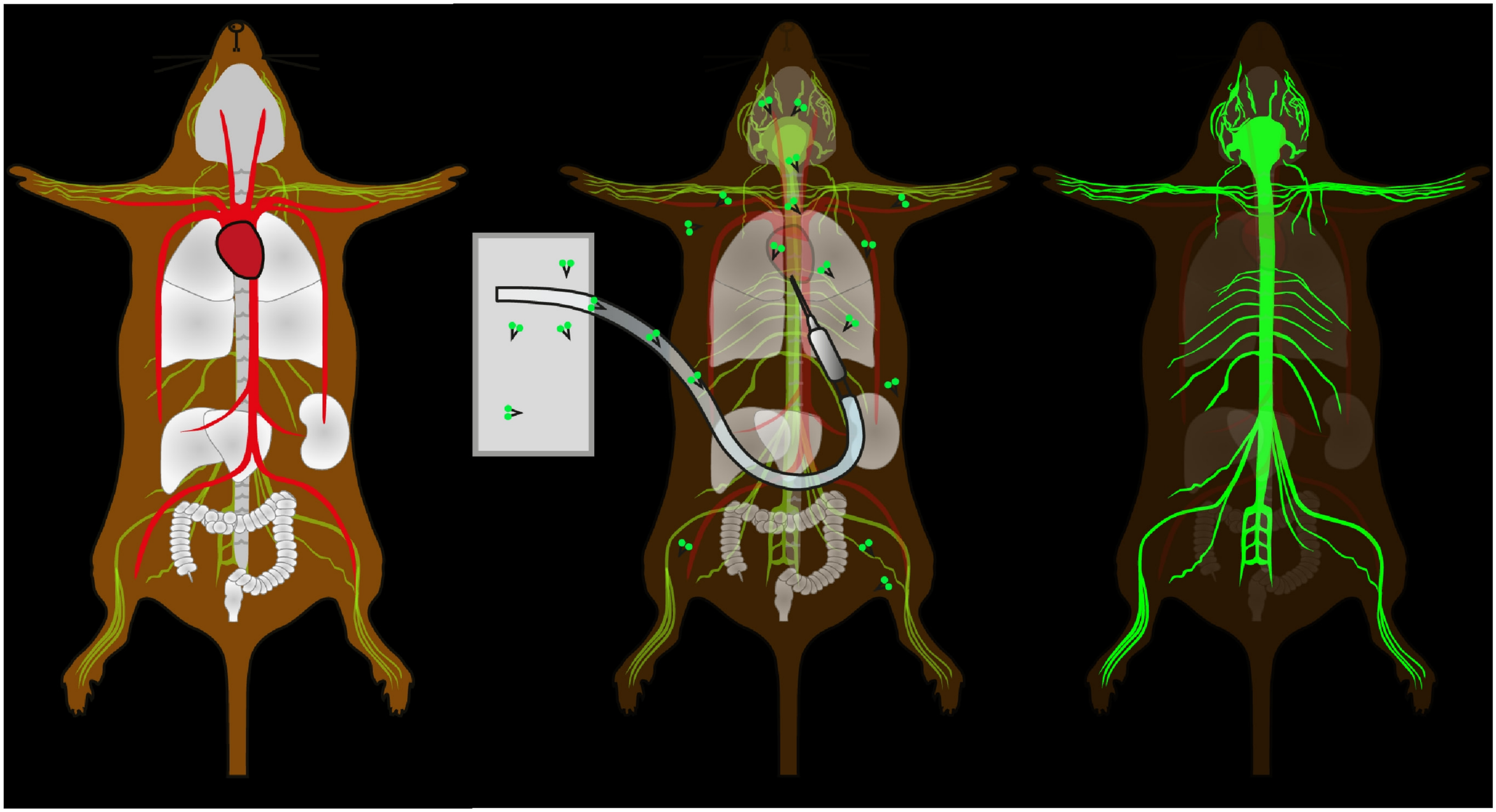

Supplementary Figure 10

Schematic illustration of whole-body vDISCO boosting method

The decolorization, decalcification, and nanoboosting steps are performed via transcardiac perfusion. After boosting, the boosted fluorescence signal becomes highly visible over the reduced background in the intact transparent animals.

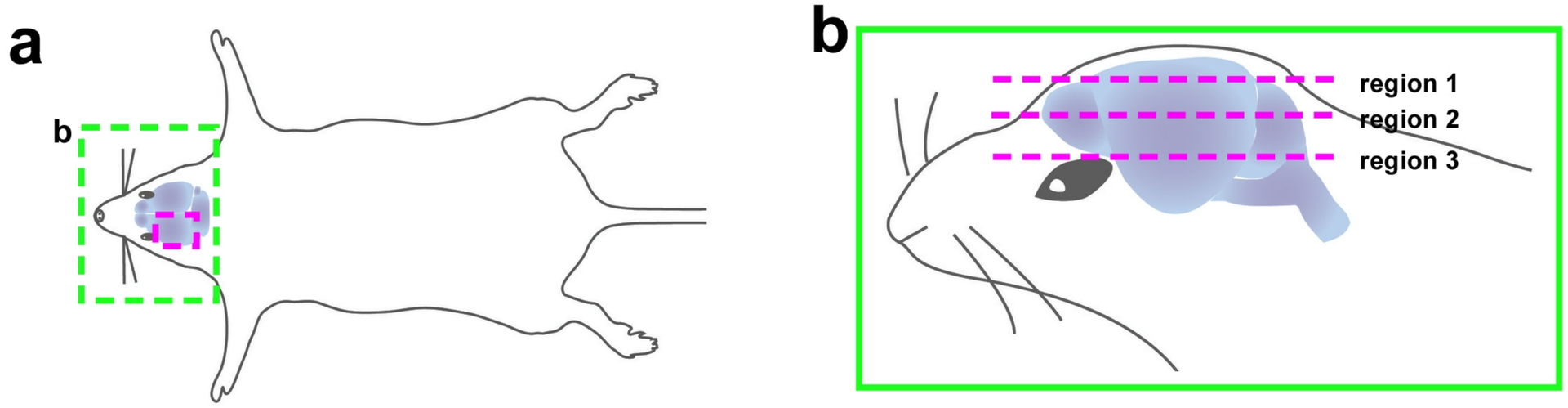

Supplementary Figure 11

Whole-body immunolabeling by vDISCO vs. other labeling methods

(**a**) Illustration showing the anatomic region (dashed magenta rectangle) of the cleared mice imaged for the comparative analysis. (**b**) Zoom-in illustration at the level of the head of the representative animal showing the 3 different z regions of interest considered for the comparative analysis. (**c**-**g**) Light-sheet images of 3 brains from 3 independent cleared animals per each group at the level of region 2 indicated in a and b showing the complete penetration of the nanobody in animals processed with vDISCO method using active high pressure perfusion (**c**) vs. the partial labeling of the surface of the brain in animals processed with vDISCO with passive incubation of the nanobody (**d**) and vs. the limited labeling of the brain in animals processed with vDISCO using active high pressure pumping of conventional anti-GFP antibody (**e**), in animals processed with iDISCO+ using active high pressure pumping of conventional anti-GFP antibody (**f**) and in animals processed with iDISCO+ using active high pressure pumping of nanobody (**g**). (**h**-**j**) Quantification of the % of stained tissue from the described protocols at the level of region 1 (**h**), region 2 (**i**) and region 3 (**j**). mean ± s.d.; n=3 2-3 months old animals per group; statistical significance (n.s.=no significant, ****$p < 0.0001$, in h: $F_{4\text{-}10}=64.26$, in i $F_{4\text{-}10}=693.0$, in j $F_{4\text{-}10}=62.19$) was assessed by one-way ANOVA followed by Dunnett´s *post hoc* test).

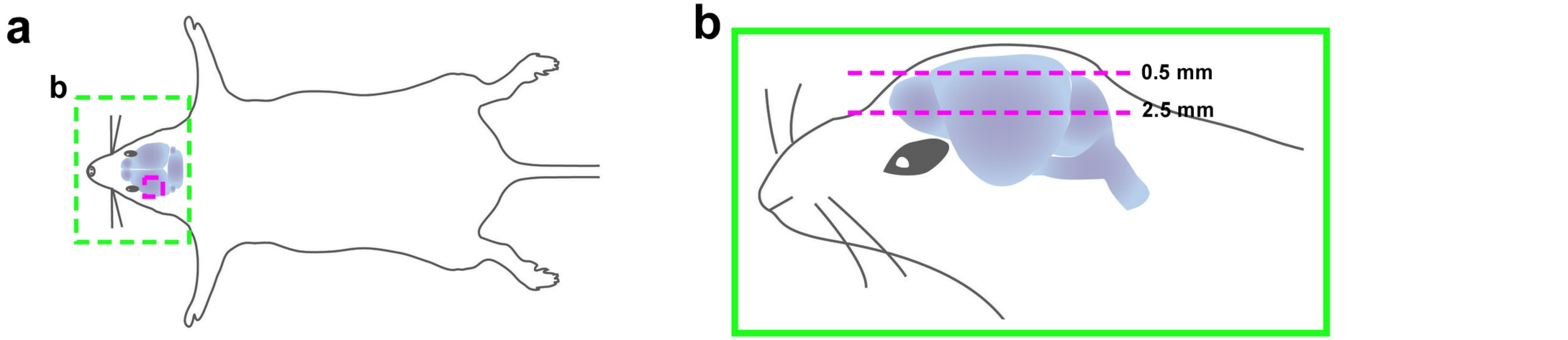

Supplementary Figure 12

Quality of imaging single cells deep in the brain through the skull by different whole-body clearing approaches
(**a**) Illustration showing the anatomic region (dashed magenta rectangle) of the cleared mice imaged for the comparative analysis. (**b**) Zoom-in illustration at the level of the head of the representative animal showing the 2 different z regions (0.5 mm and 2.5 mm deep from the dorsal brain surface) considered for the comparative analysis. (**c**-**g**) To compare different clearing methods, whole-bodies of 2 months old CX3CR1$^{GFP/+}$ mice were cleared by PARS (**c**), CUBIC-R (**d**), uDISCO (**e**), PEGASOS (**f**) and vDISCO (**g**). After clearing, the whole-heads of mice with intact skull were taken for light-sheet microscopy for signal comparison. Representative images and normalized signal profiles at 0.5 mm and 2.5 mm depth indicate that vDISCO is the only method providing reliable detection of microglia cells through the intact skull. Similar results were observed from 3 independent mice per group. Among all the clearing methods tested, PARS, PEGASOS and vDISCO were characterized by a decalcification step using EDTA solutions.

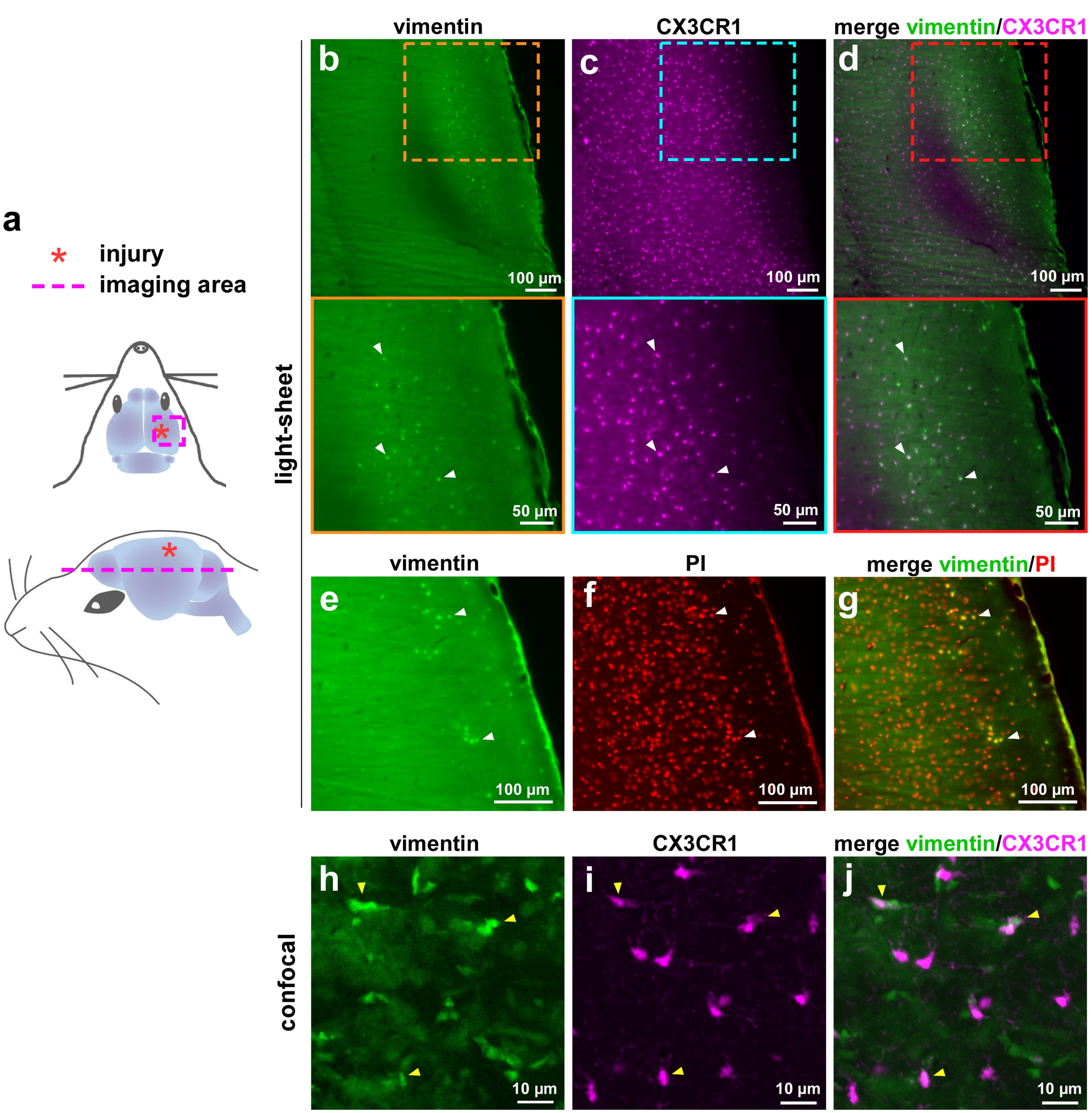

Supplementary Figure 13

vDISCO labeling of vimentin expressing cells using anti-vimentin nanobody

(**a**) Illustration showing the injury location of the brain trauma (red asterisk) and the imaging area (magenta dashed line). (**b**-**d**) Light-sheet imaging of a mouse brain from traumatic brain injured 4 months old CX3CR1$^{GFP/+}$ animal 1 month after the injury: vimentin was labeled using anti-vimentin 488-nanobooster (green), in which the autofluorescence of the tissue is much higher than in the far-red spectrum. (**b**) CX3CR1 GFP+ cells were boosted using anti-GFP 647-nanobooster (magenta) (**c**), the colocalization of CX3CR1 GFP+ immune cells expressing vimentin is visible in white in the merge panel (**d**). The colored rectangles show zoom-in images of the dashed regions in b-d. White arrow-heads indicate examples of colocalizing signal in cells. (**e**-**g**) Light-sheet imaging of the same brain from the TBI CX3CR1$^{GFP/+}$ animal in b-d: vimentin is shown in green (**e**), while all nuclei of the cells were labeled using propidium iodide (PI) (red) (**f**), the colocalization of the signal in cells expressing vimentin and stained with PI is visible in yellow in the merge panel (**g**). White arrow-heads indicate examples of colocalizing signal in cells. (**h**-**j**) Confocal imaging of the mouse brain in b-d showing vimentin (green) (**h**) and CX3CR1 GFP+ cells (magenta) (**i**), the colocalization of CX3CR1 GFP+ immune cells expressing vimentin is visible in white and indicated by yellow arrow-heads in the merge panel (**j**). Single experiment.

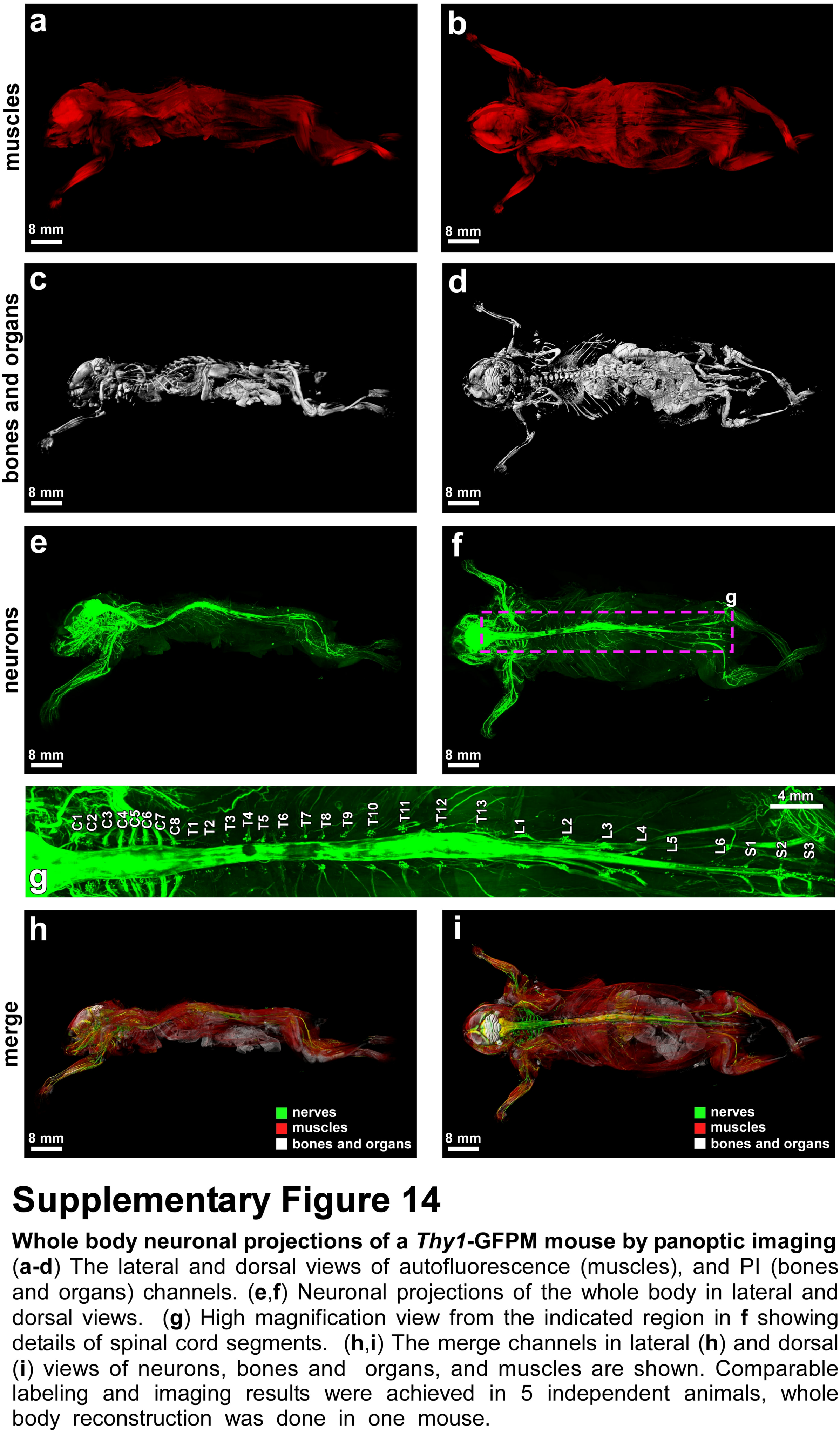

Supplementary Figure 14

Whole body neuronal projections of a *Thy1*-GFPM mouse by panoptic imaging
(**a-d**) The lateral and dorsal views of autofluorescence (muscles), and PI (bones and organs) channels. (**e**,**f**) Neuronal projections of the whole body in lateral and dorsal views. (**g**) High magnification view from the indicated region in **f** showing details of spinal cord segments. (**h**,**i**) The merge channels in lateral (**h**) and dorsal (**i**) views of neurons, bones and organs, and muscles are shown. Comparable labeling and imaging results were achieved in 5 independent animals, whole body reconstruction was done in one mouse.

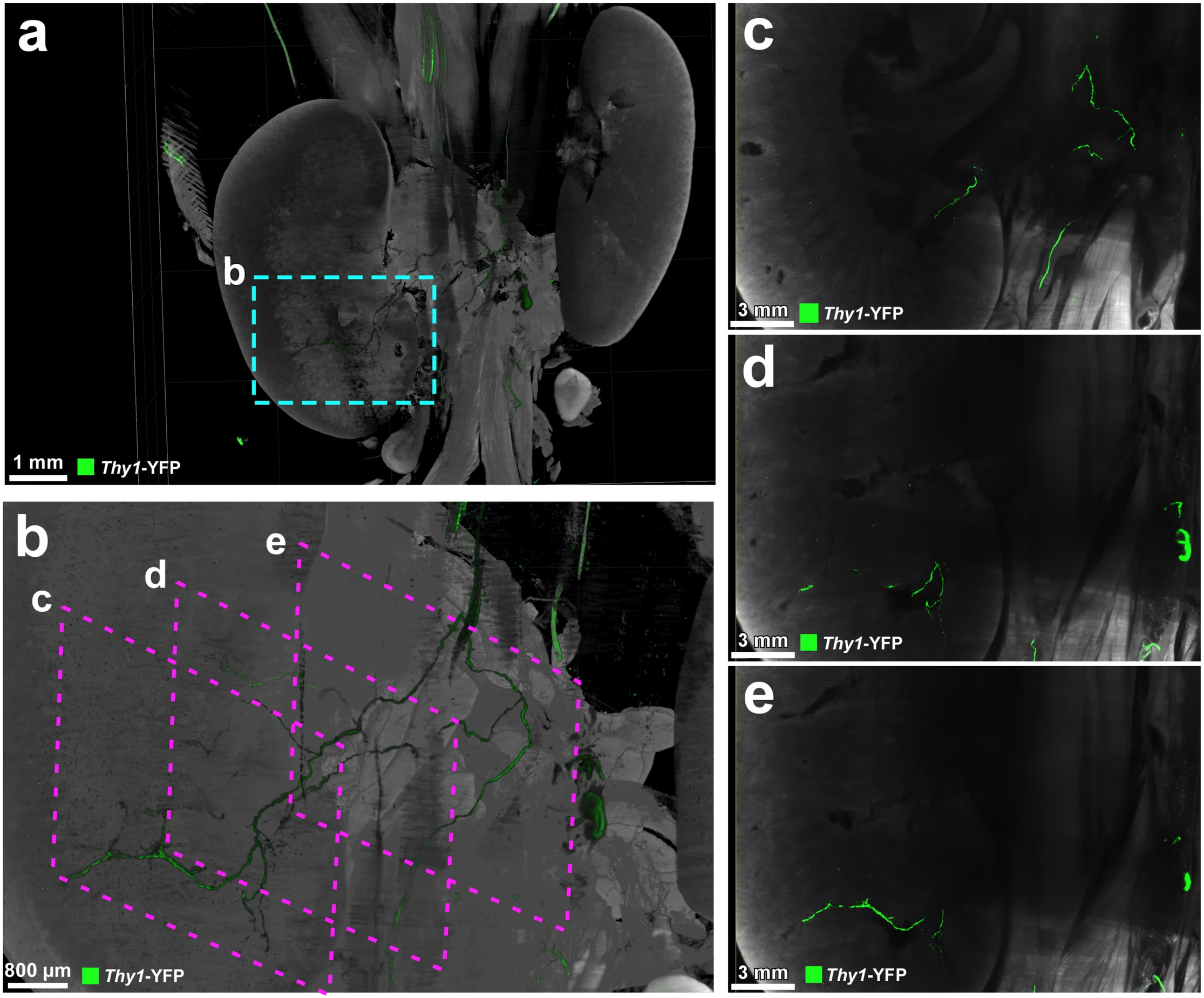

Supplementary Figure 15

Peripheral nerves innervating kidneys in *Thy1*-YFPH mouse

(**a**) 3D visualization of nerves innervating the kidneys of a 7 months old *Thy1*-YFPH animal. (**b**) Zoom image from the marked region in **a**. (**c**-**e**) 2D projection images of the kidney at the indicated depths in **b**. Single experiment.

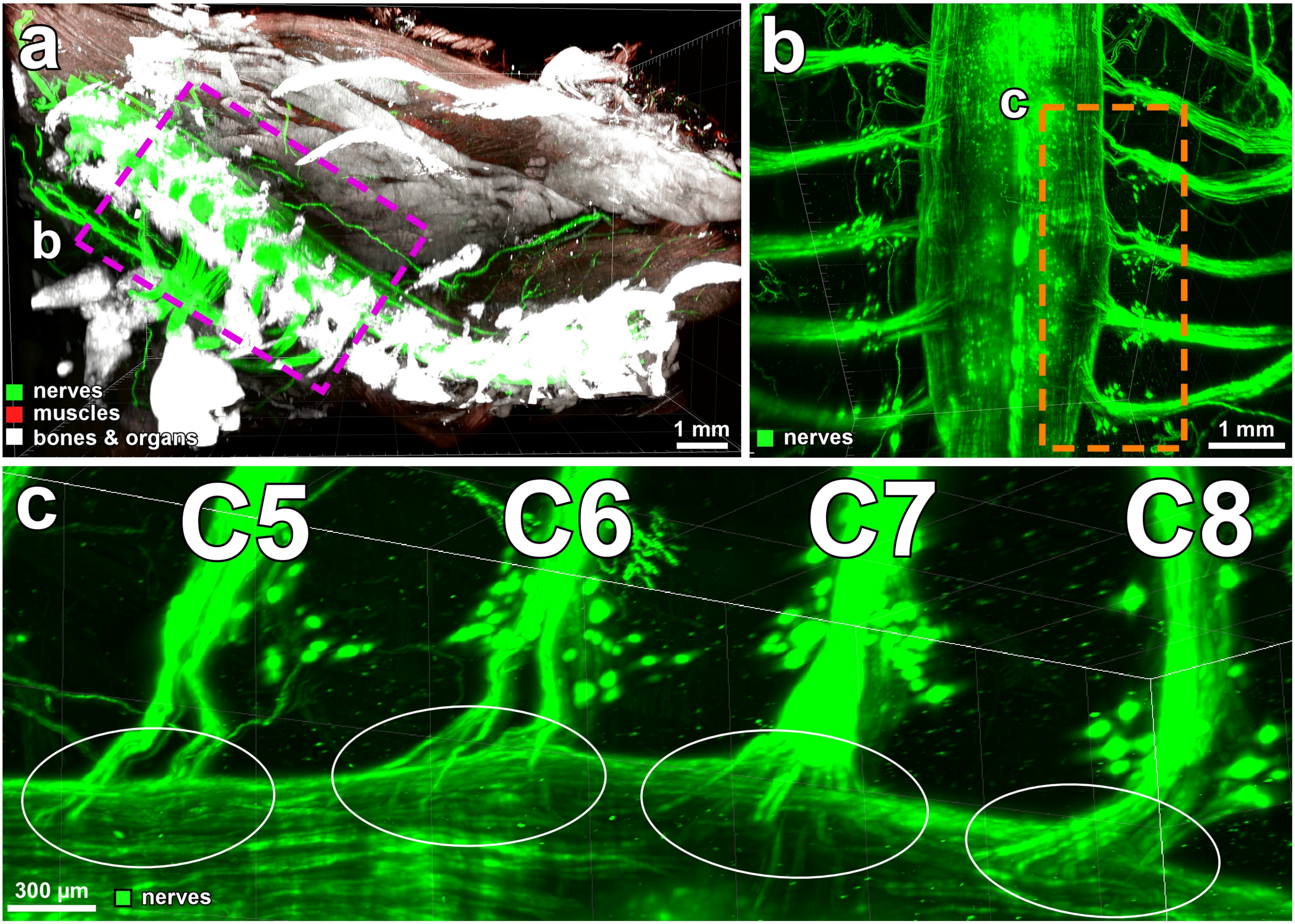

Supplementary Figure 16

Upper torso and individual spinal cord roots

(**a**) Panoptic imaging of the upper torso of the 6 weeks old transparent mouse showing individual spinal cord roots. The bones and organs are in white, mostly the muscles are visible in autofluorescence channel and displayed in red, and the nerves are in green. (**b**) High magnification view from the region indicated in **a** showing only nerve signal (ventral roots). (**c**) High magnification view from the region indicated in **b** demonstrating non-overlapping entry of axons in C5-C8 ventral spinal cord segments (white circles). Comparable labeling and imaging results were achieved in 5 independent animals.

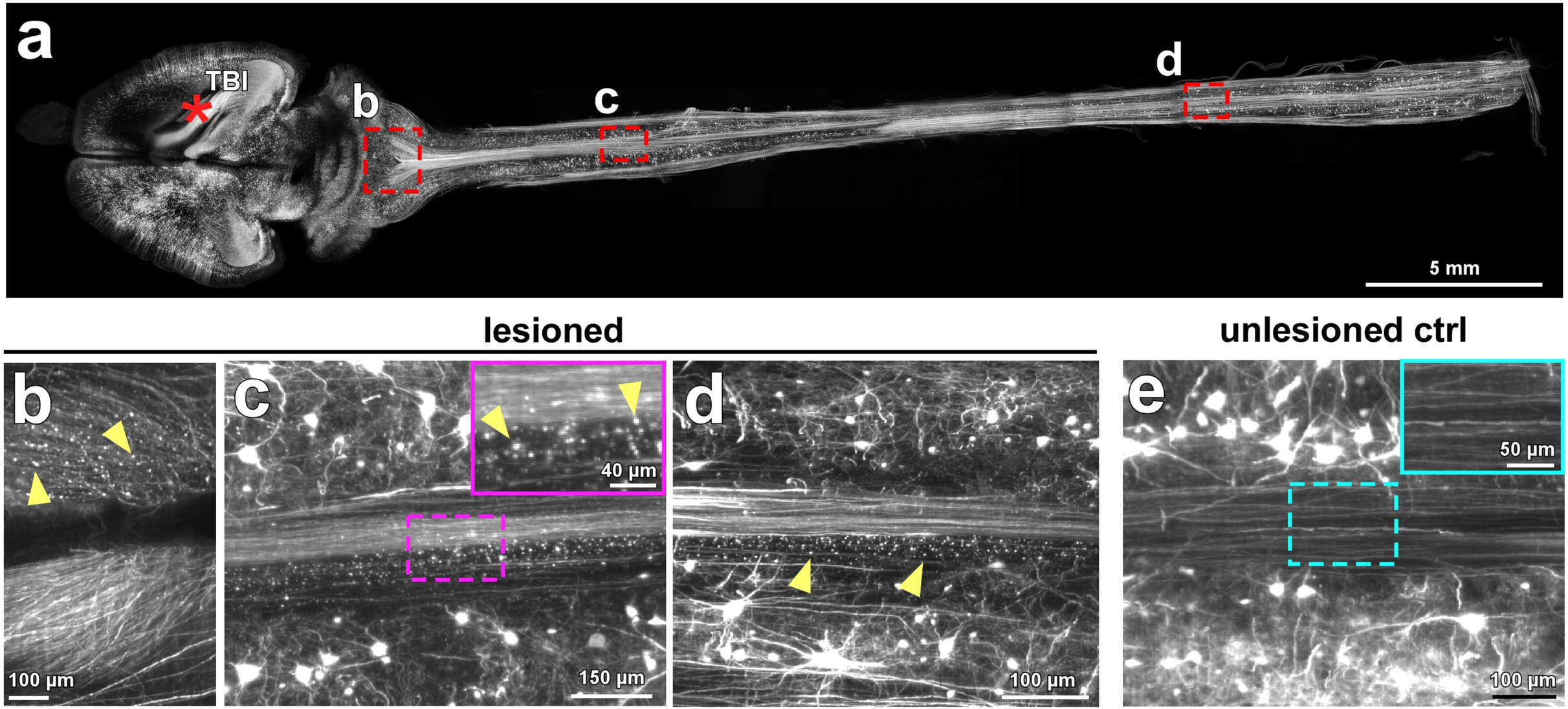

Supplementary Figure 17

TBI induces the degeneration of descending motor axons in the central nervous system

(**a**) To investigate a potential degeneration of the descending motor axons upon TBI, we applied vDISCO on the intact CNS (brain and spinal cord) from *Thy1*-GFPM mice already 1 week after TBI. (**b-d**) High magnification images coming from the indicated spinal cord regions marked in a. The fragmentation (yellow arrow-heads) of the descending motor axons ipsilaterally in the brainstem before the decussation (**b**), and contra-laterally after decussation is evident throughout the spinal cord (**c,d**). (**e**) An unlesioned spinal cord view at the same region shown in the lesioned animal in d. Similar results were observed from 2 independent animals.

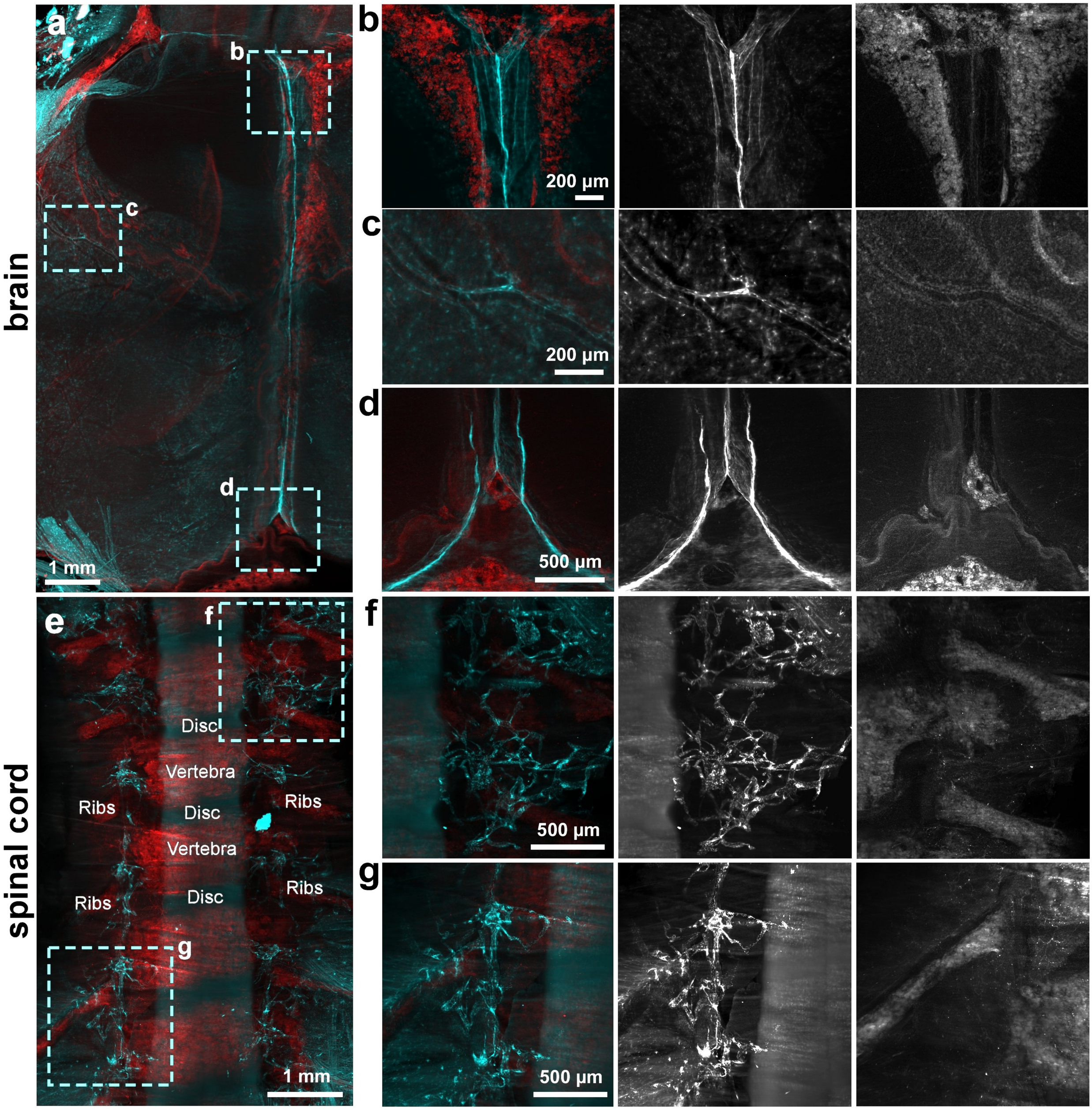

Supplementary Figure 18

Meningeal lymphatic vessels through transparent skull and vertebra by vDISCO

After applying vDISCO pipeline, the 4 weeks old *Prox1*-EGFP mouse was imaged with light-sheet microscopy. Prox1 and PI channels are shown in merge and separate views. (**a-d**) *Prox1*-EGFP mouse head showing the brain lymphatic vessels (cyan) along the sagittal sinus (**b**), pterygopalatine artery (**c**) and transverse sinus (**d**) (similar results were observe from 5 independent mice). (**e-g**) Images from the thoracic region of the spine show the lymphatic vessels (cyan) in the spine region (single experiment).

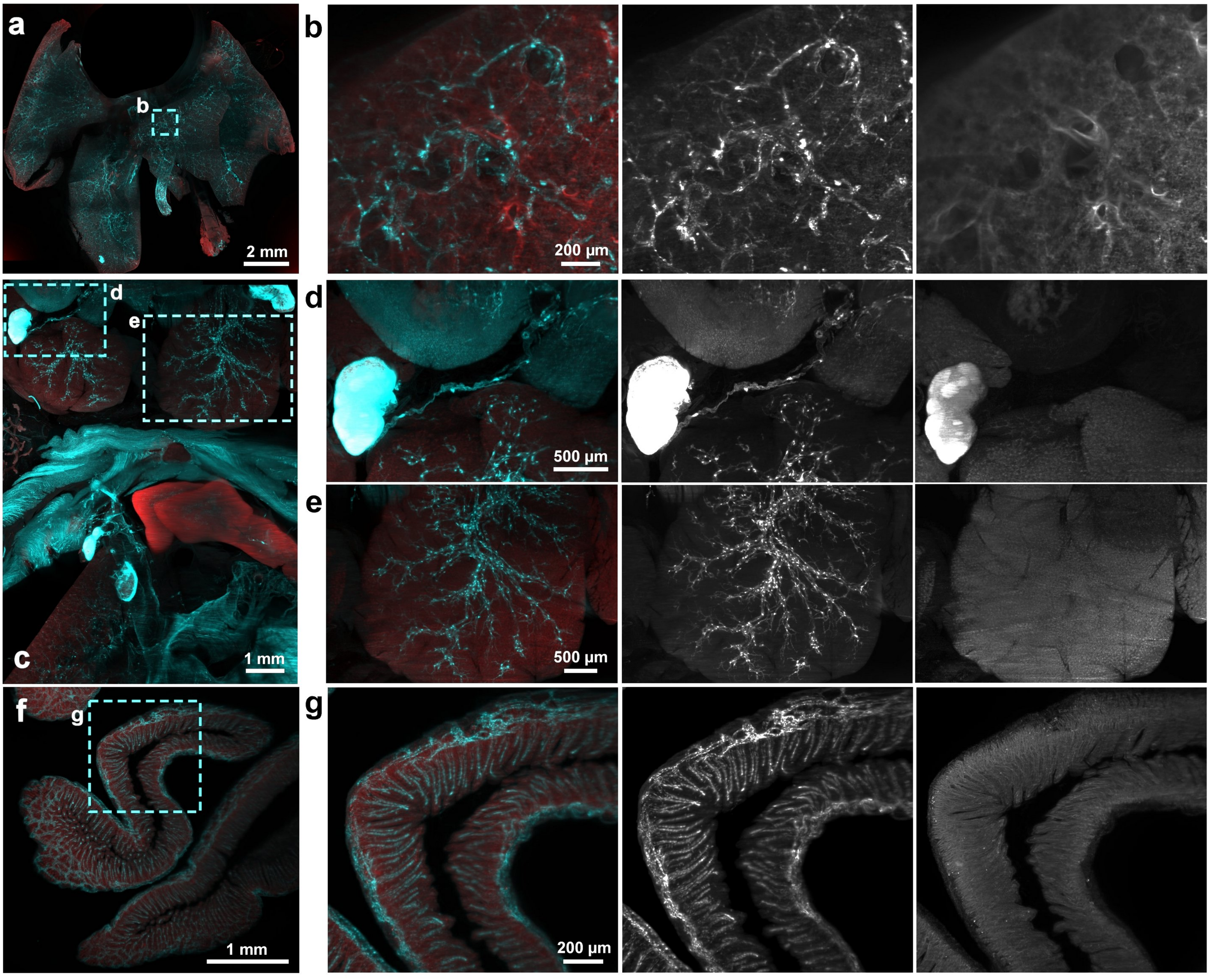

Supplementary Figure 19

Lymphatic vessels in internal organs by vDISCO

After applying vDISCO pipeline, the 4 weeks old *Prox1*-EGFP mouse was imaged with light-sheet microscope (single experiment). Prox1 and PI channels are shown in merge and separate views. The lymphatic vessels (cyan) in lungs (**a-b**), in cervical lymph node (**c**,**d**), in salivery gland (**c**,**e**) and in intestine (**f**,**g**) are evident. See also Supplementary Video 6.

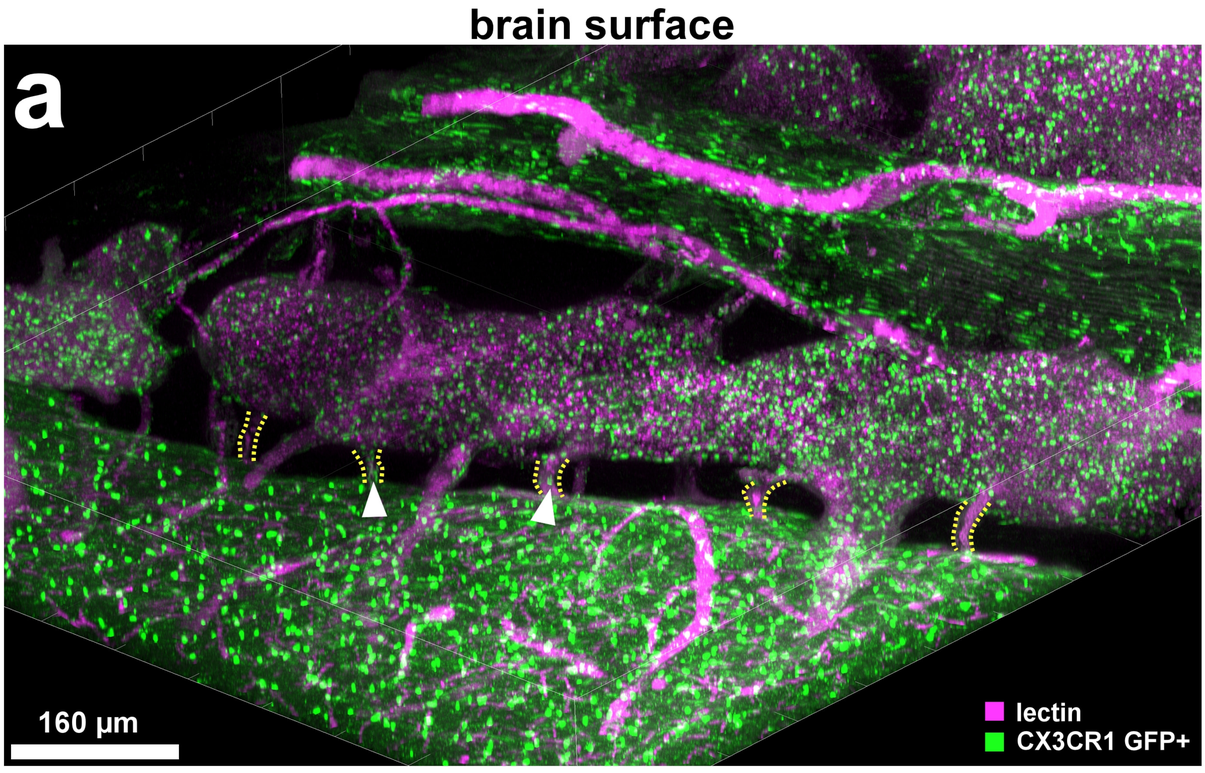

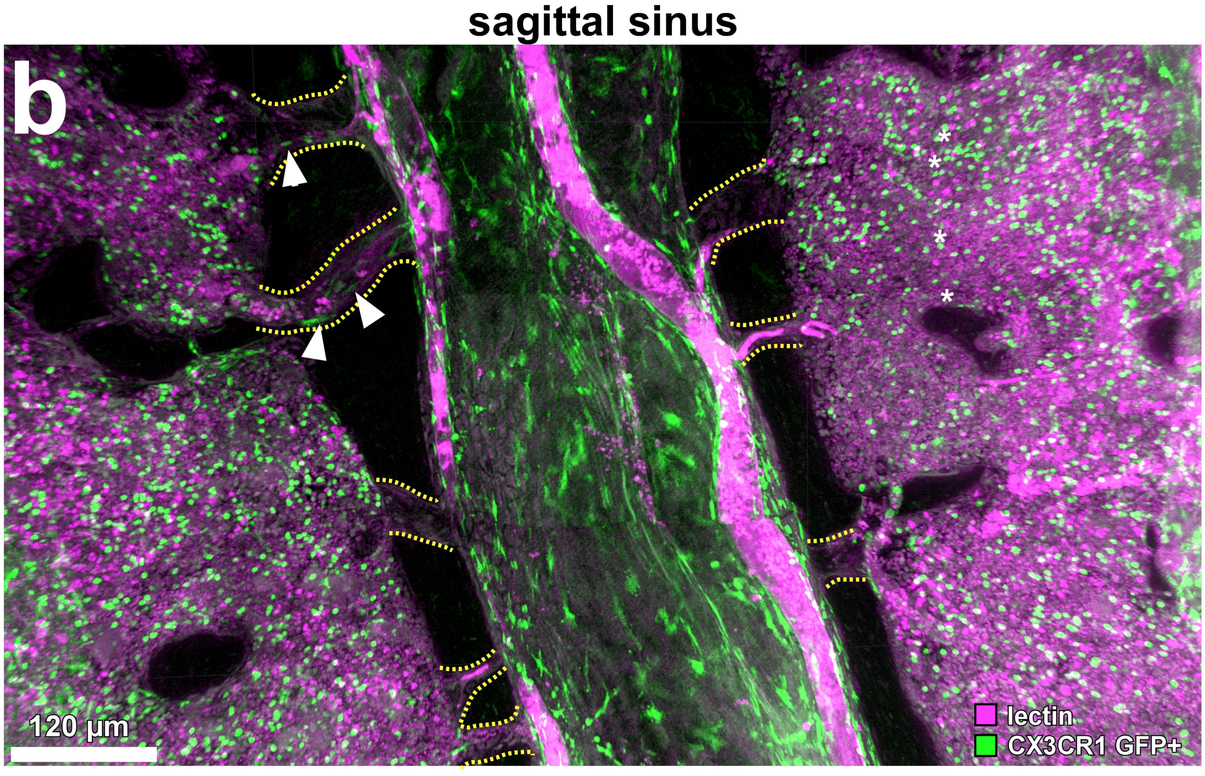

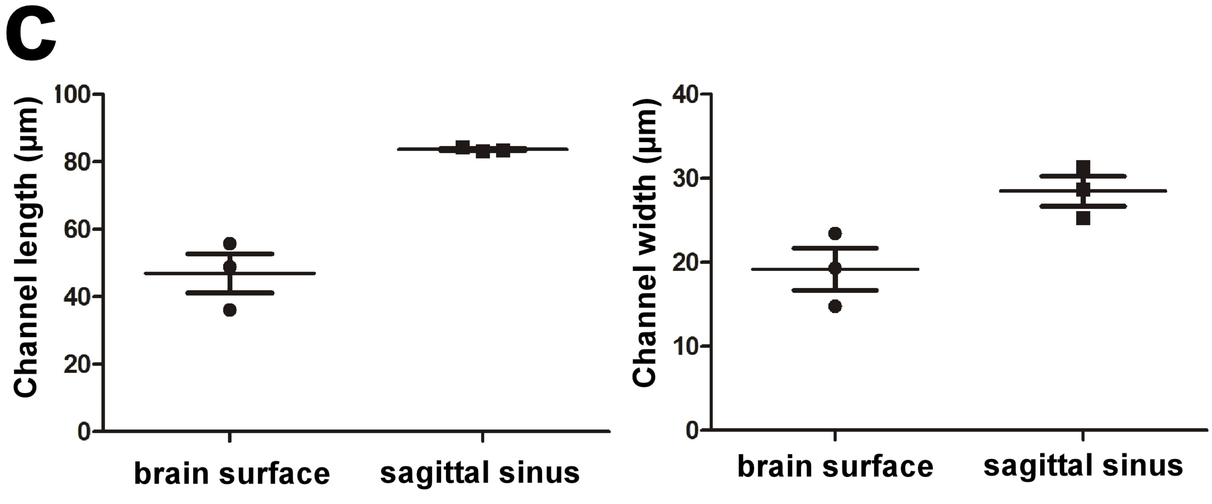

Supplementary Figure 20

Structural features of short skull-meninges connections (SMCs)

(**a**,**b**) 3D confocal images of brain-skull interface. A 4 months old CX3CR1$^{GFP/+}$ mouse (CX3CR1 GFP+ cells in green) was injected with lectin dye (magenta). Vascular connections between the skull marrow and meninges at the brain surface (**a**) and sagittal sinus (**b**) are visible, including the CX3CR1 GFP+ cells (white-arrow heads) in the connections (similar results were observed from 3 independent mice). See also Supplementary Video 9. (**c**) Quantifications of length and width of the SMCs at sagittal sinus and brain surface (mean ± SEM; n=3 animals per group).

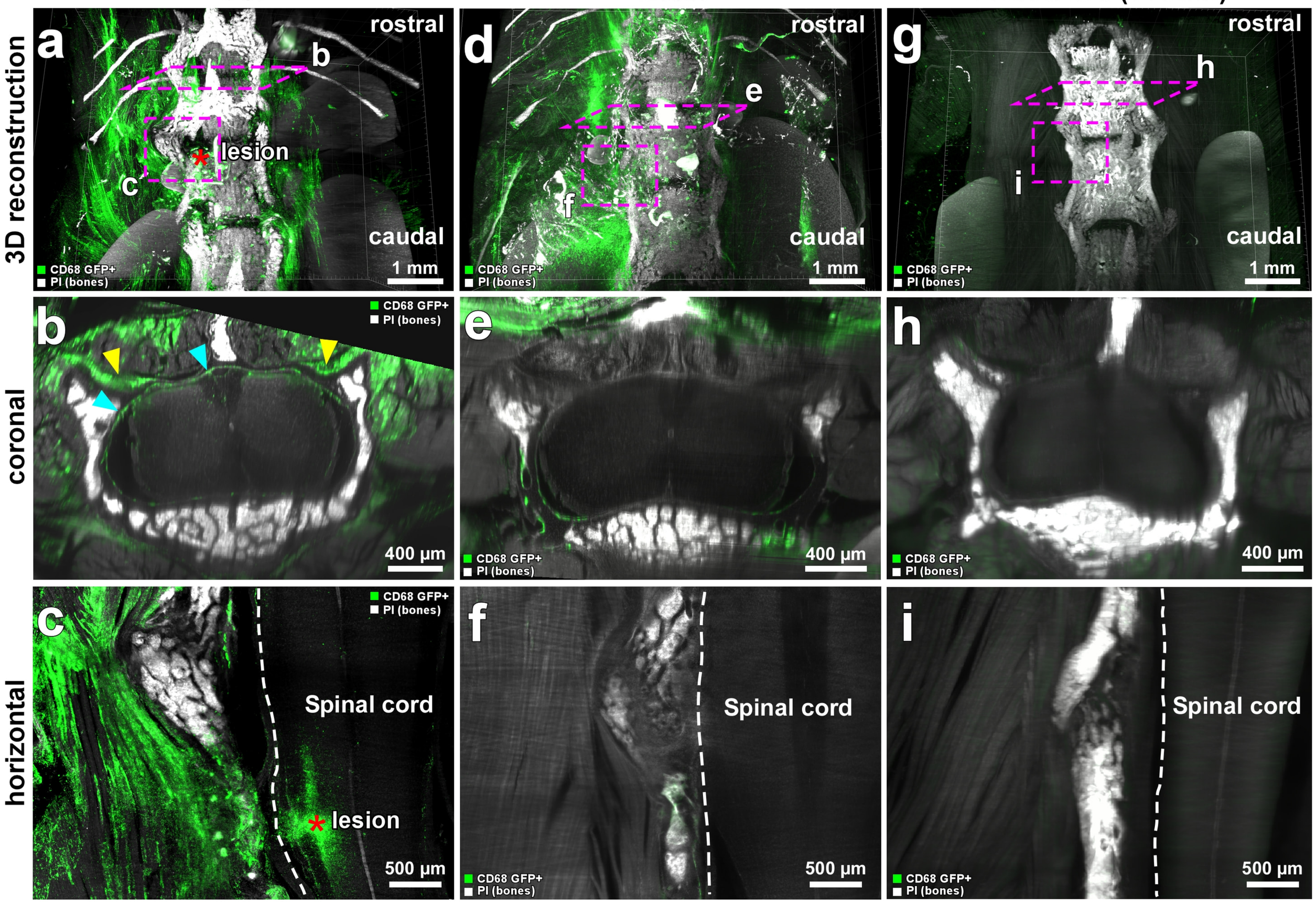

Supplementary Figure 21

Immune cell activation and invasion induced by spinal cord injury

3D visualization of spinal cord from 3 months old *CD68*-EGFP transgenic mice with spinal cord injury (**a**-**c**) compared to mice with sham surgery (**d**-**f**) and unlesioned controls (**g**-**i**). CD68 GFP+ cells are shown in green and PI labeled bones in white. Red asterisks indicate the lesion site. Increased CD68 GFP+ cells throughout the muscles, spinal cord roots (yellow arrow-heads) and meninges (cyan arrow-heads) are evident in the injured spinal cord (**a**-**c**) compared to the controls (**g**-**i**). In the group with sham surgery, the CD68 GFP+ cells increased in the muscles but not in the spinal cord (similar results were observed from 3 independent mice per group). See also Supplementary Video 11.

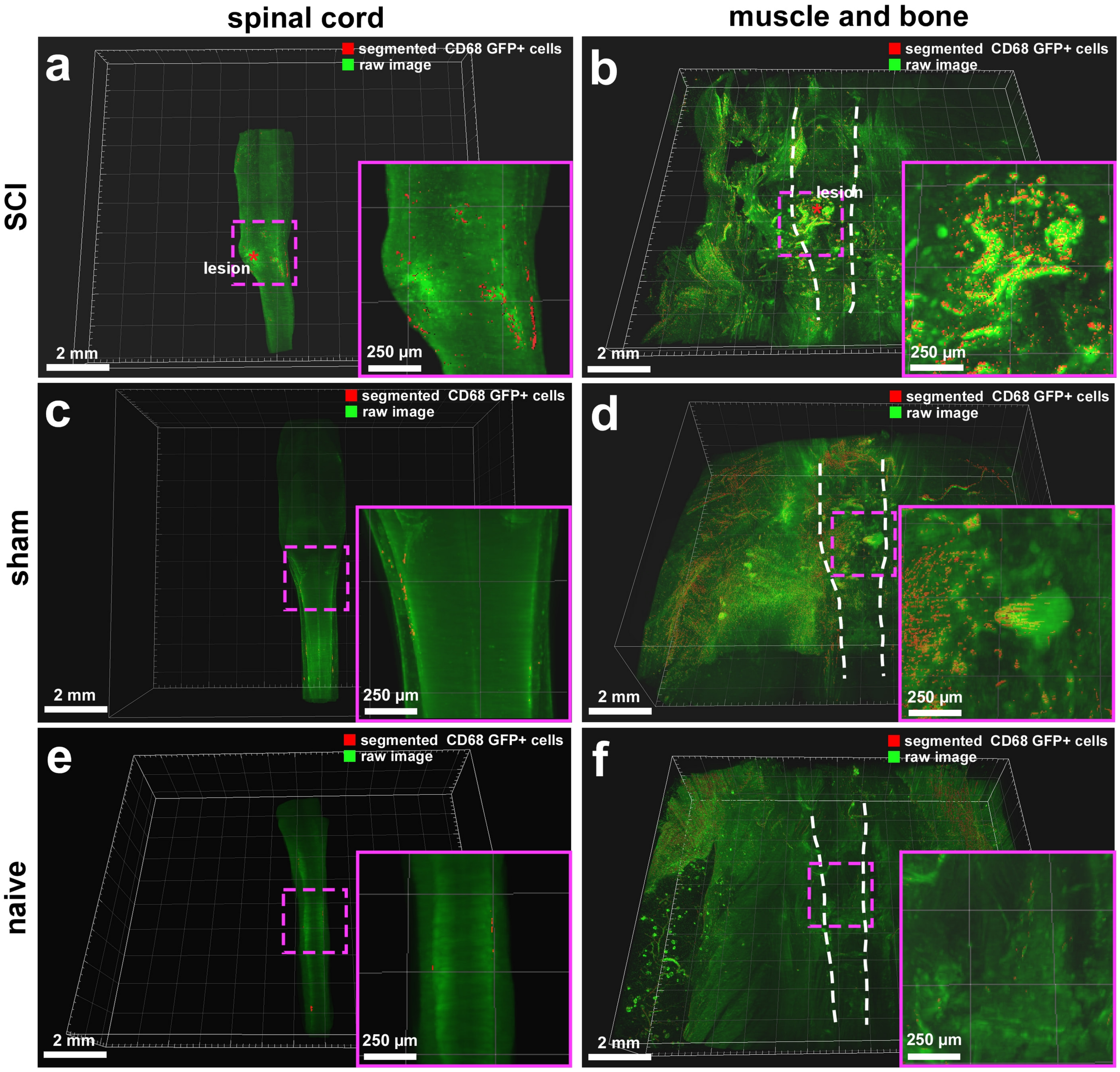

Supplementary Figure 22

CD68 GFP+ cell number increased significantly both in spinal cord and peripheral tissues after spinal cord injury (SCI)

(**a**-**f**) 3D visualization of the spine region from 3 months old *CD68*-EGFP mice with SCI (**a**,**b**) vs. mice with sham surgery (**c**,**d**) and naive mice (**e,f**) cleared by vDISCO and imaged by light-sheet microscope. To better visualize the region, spinal cords (**a**,**c** and **e**) were segmented out from their locations in the surrounding tissues (muscle and bone) (**b**,**d** and **f**) using Fiji and afterwards CD68 GFP+ cells were segmented (red) and quantified by IMARIS (similar results were observed from 3 independent mice per group). (**g**) Quantification of CD68 GFP+ cells in spinal cord showing significant cell number increase after SCI compared to sham and naive animals. While CD68 GFP+ cell number increased significantly in surrounding tissue (muscle and bone) in SCI group compared to naive animals (mean ± SEM; n=3 animals per group; statistical significance (for spinal cord, $F_{2,6}$=17.22, SCI vs. sham ***p*=0.0077, SCI vs. naive ***p*=0.0041 and sham vs. naive ns=0.8049. For muscle and bone, $F_{2,6}$=10.05, SCI vs. sham ns=0.2273, SCI vs. naive **p*=0.0101 and sham vs. naive ns=0.0905) was assessed by one-way ANOVA followed by Tukey multiple comparison Test).

DISSECTED ORGANS

steps

tissue type / passive incubation (with shaking)	whole organs such as brain, heart or spleen	soft and porous organs such as gut, lungs or thymus	small organs such as adrenal glands, lymphnodes, organoids or 1 mm slices
pretreatment with permeabilization solution at 37°C	1-2 days	overnight	6 hours
incubation with immunostaining solution at 37°C	10-14 days	4-5 days	3-4 days
washing with washing solution at room temperature	2 hours x 4 times (optionally last step overnight)	1.5 hours x 4 times	1 hour x 4 times
PBS washing at room temperature	2 hours x 4 times	1.5 hours x 4 times	1 hour x 4 times
DISCO clearing			
50% THF at room temperature	1-2 hours	1 hour	1 hour
70% THF at room temperature	1-2 hours	1 hour	1 hour
80% THF at room temperature	1-2 hours	1 hour	1 hour
100% THF at room temperature	1 hour and overnight	1 hour and overnight	1 hour and 5 hours
100% DCM at room temperature	1 hour	45 minutes	30 minutes
BABB at room temperature	overnight	> 6 hours	> 4 hours
cost per sample	~25-30 $	~15-20 $	~6-8 $
imaging time (light-sheet microscopy)	~1.5-3 hours	~3-6 hours	~0.5-1.5 hours

WHOLE BODY

steps

	modality	timing	temperature
PBS washing	active perfusion	overnight	at room temperature
decolorization with 25% CUBIC#1 in PBS	active perfusion	12 hours x 4 times	at room temperature
PBS washing	active perfusion	3 hours x 3 times	at room temperature
decalcification with 10% of EDTA in PBS pH8-9	active perfusion	2 days	at room temperature
PBS washing	active perfusion	3 hours x 3 times	at room temperature
pretreatment with permeabilization solution	active perfusion	12 hours	at room temperature
boosting with immunostaining solution	active perfusion	6 days	with infrared lamp (up to 30°C)
boosting with immunostaining solution	passive shaking	2 days	at 37°C
wash with washing solution	active perfusion	3 hours x 3 times	at room temperature
PBS washing	active perfusion	3 hours x 3 times	at room temperature
DISCO clearing			
50% THF in distilled water	passive shaking	12 hours	at room temperature
70% THF in distilled water	passive shaking	12 hours	at room temperature
80% THF in distilled water	passive shaking	12 hours	at room temperature
100% THF	passive shaking	12 hours x 2 times	at room temperature
100% DCM	passive shaking	3 hours	at room temperature
BABB	passive shaking	> 12 hours	at room temperature
cost per animal	~180-200 $		
imaging time (light-sheet microscopy)	~3-5 days		

permeabilization solution: 1.5% goat serum , 0.5% Triton X-100, 0.5 mM Methyl-beta-cyclodextrin, 0.2% trans-1-Acetyl-4-hydroxy-L-proline, 0.05% Sodium Azide in 0.1 M PBS

washing solution: 1.5% goat serum , 0.5% Triton X-100, 0.05% Sodium Azide in 0.1 M PBS

immunostaining solution: permeabilization solution + nanobooster

THF: tetrahydrofuran
DCM : dichloromethane
BABB: benzyl alcohol + benzyl benzoate (1:2) in volume
CUBIC#1: 25 wt% urea , 25 wt% N,N,N´,N´-tetrakis (2-hydroxypropyl)ethylenediamine, 15 wt% Triton X-100 in 0.1 M PBS

Supplementary Table 1

Notes for vDISCO protocol

The timing for each experimental step can be shortened or extended based on tissue size to improve nanobooster penetration or clearing performance. We found that active (perfusion mediated) whole-body boosting provides more homogeneous and even nanobooster staining compared to passive staining of dissected organs e.g. the brain, if the perfusion is done properly. The costs were estimated only based on the reagents and considering organs from transgenic mouse lines that highly express GFP, such as *Thy1*-GFPM. If other lines (which express less GFP) are used, the amount of nanobooster needed for the protocol can be reduced and the cost might reduce significantly as well. The imaging time has been estimated considering the imaging only with one channel using the Ultramicroscope II (LaVision BioTec) with a 4x objective and it can significantly vary based on many factors: z-step, magnification, different microscope version etc. More information available at www.discotechnologies.org/vDISCO.

FIGURES		SYSTEM	OBJECTIVE SPECIFICATIONS					ACQUISITION PARAMETERS			DATA SIZE
			Magnification	NA	RI	WD	Zoom	Image pixel size	z-step	type	
Figures											
1	a-f	UM II	4X corr.	0.28	1.56	10mm		1.625µmx1.625µm	4µm	single slice	(a)24.8GB, (e)34.7GB
	g,h	UM II	4X corr.	0.28	1.56	10mm		1.625µmx1.625µm	(i)8µm, (j)12µm	single slice	(i)29.5GB, (j)9.90GB
	i	UM II	4X corr.	0.28	1.56	10mm		1.625µmx1.625µm	4-12µm	quantification on single slice	67GB
	j,l,n	UM II	4X corr.	0.28	1.56	10mm		1.625µmx1.625µm	8-10 µm	single slice	(j,l)12.8GB, (n)6.94GB
	k,m	UM II	Oly. 25X	0.95	1.31-1.52	4mm		0.26µmx0.26µm	4µm	single slice	(m)1.37GB, (o)222MB
	o	UM II	4X corr.	0.28	1.56	10mm		1.625µmx1.625µm	8µm	single slice	456GB
2	b-d	UM II -MVX10	Oly. 1X	0.25	1.0	65mm	0.63x	10.32µmx10.32µm	8µm	3D reconstruction	3.27TB
	f-i	UM II -MVX10	Oly. 2X	0.5	1.33/1.56	6mm	1.6x	2.03µmx2.03µm	6µm	3D reconstruction	1.5TB
3	d	UM II	4X corr.	0.28	1.56	10mm		1.625µmx1.625µm	8µm	3D reconstruction	140GB
	e,g	LSM880	Leica 25x	0.95	1.33	2.5mm		0.67µmx0.67µm	4µm	(e) 3D reconstr., (g) single slice	3.89GB
	f,h	LSM880	Leica 25x	0.95	1.33	2.5mm		0.67µmx0.67µm	4µm	96µm thick projection	same data from Fig.6e,g
	j	UM II -MVX10	Oly. 2X	0.5	1.33/1.56	6mm	0.8x	4.06µmx4.06µm	8µm	1440µm thick projection	117GB
	k	LSM880	Leica 25x	0.95	1.33	2.5mm		0.4µmx0.4µm	2.50 µm	180µm thick projection	2.45GB
4	a-d	UM II -MVX10	Oly. 1X	0.25	1.0	65mm	(a,c)1.25x, (b,d)0.63x	(a,c)5.2µmx5.2µm, (b,d)10.32µmx10.32µm	8µm	entire scan projection	(a,c)52.2GB, (b,d)16.8GB
	c,d (yellow, green rectangles)	UM II	Zeiss 20x	1	1.45	5.6mm		0.325µmx0.325µm	2µm	(c)824µm, (d)430µm thick projections	(c)64.8GB, (d)62.7GB
	e	UM II -MVX10	Oly. 2X	0.5	1.33/1.56	6mm	2.5x	1.3µmx1.3µm	8µm	quantification entire scan projection	1TB
5	b	UM II -MVX10	Oly. 2X	0.5	1.33/1.56	6mm	1x	3.25µmx3.25µm	8µm	1.6mm thick projection	105GB
	c-e	UM II -MVX10	Oly. 2X	0.5	1.33/1.56	6mm	2x	1.625µmx1.625µm	10µm	(c)600µm, (d) 500µm, (e)400µm thick projections	(c,e) 42.5GB, (d) 28.4GB
	f	UM II -MVX10	Oly. 2X	0.5	1.33/1.56	6mm	2x	1.625µmx1.625µm	7µm	3D reconstruction	87GB
	g,h	UM II	Zeiss 20x	1	1.45	5.6mm		0.325µmx0.325µm	3µm	15µm thick projections	552GB
	i,j	UM II -MVX10	Oly. 2X	0.5	1.33/1.56	6mm	2x	1.625µmx1.625µm	10µm	single slices	(i)102GB, (j)86.5GB
6	a	UM II	4X corr.	0.28	1.56	10mm	2x	0.8µmx0.8µm	6µm	3D reconstruction	5.8GB
	b-d	UM II -MVX10	Oly. 1X	0.25	1.0	65mm	3.2x	2µmx2µm	8µm	80µm thick projections	5.5GB
	e,f	UM II -MVX10	Oly. 1X	0.25	1.0	65mm	0.63x	8µmx8µm	3µm	single slices	77.9GB
	g,h	UM II -MVX10	Oly. 2X	0.5	1.33/1.56	6mm	1.6x	2µmx2µm	8µm	40µm thick projections	(g)349GB, (h)550GB
	i	UM II -MVX10	Oly. 2X	0.5	1.33/1.56	6mm	1.6x	2µmx2µm	8µm	quantification 40µm projection	1.38 TB for 6 samples
Sup. Figures											
S1	a	UM II -MVX10	Oly. 1X	0.25	1.0	65mm	1x	6.5µmx6.5µm	10µm	single slice	9.37GB
S2	a-f	UM II	4X corr.	0.28	1.56	10mm		1.625µmx1.625µm	10-12 µm	40-48µm thick projection	(a,b,c)30.2GB, (d,e,f) 31.7 GB
	g	UM II	4X corr.	0.28	1.56	10mm		1.625µmx1.625µm	8-16 µm	quantification single slide	71.31GB
S3	a-d	AxioZoom	Zeiss 1X	0.25	1.0	56mm		(a,b)1.14µmx1.14µm, (c,d) 1.82µmx1.82µm	n.a.	single slice	5.46MB x 4= 21.84MB
	e,f	UM II	4X corr.	0.28	1.56	10mm		1.625µmx1.625µm	10µm	50µm thick projection	(e)43.01GB, (f)5.93GB
	g-i	UM II	4X corr.	0.28	1.56	10mm		1.625µmx1.625µm	10µm	quantification single slice	same data from Fig.S3e,f
S4	a-e	UM II	Zeiss 20x	1	1.45	5.6mm		0.325µmx0.325µm	2µm	800 µm thick projection, 3D reconstr.	193.1GB
S5		UM II	Zeiss 20x	1	1.45	5.6mm		0.325µmx0.325µm	2µm	800 µm thick projection, 3D reconstr.	same data as Fig.S4
S6	a-c	UM II	4X corr.	0.28	1.56	10mm		1.625µmx1.625µm	4µm	3D reconstr. 8µm, thick projection	2.1GB
S7	a,h-k	UM II	4X corr.	0.28	1.56	10mm		1.625µmx1.625µm	10µm		118.1 GB
	d,g	UM II	4X corr.	0.28	1.56	10mm		1.625µmx1.625µm	3µm	single slice	32 GB
S9	c	AxioZoom	Zeiss 1X	0.25	1.0	56mm		6.49µmx6.49µm, zoom in 0.405µmx0.405µm	n.a.	single slice	106MB
S11	c-j	UM II -MVX10	Oly. 2X	0.5	1.33/1.56	6mm	0.63x	5.16µmx5.16µm	8-20µm	quantification on single slice	117.1GB
S12	c-g	UM II	4X corr.	0.28	1.56	10mm		1.625µmx1.625µm	8µm	single slices	10-50GB for each sample
S13	b-g	UM II -MVX10	Oly. 2X	0.5	1.33/1.56	6mm	4x	0.81µmx0.81µm	6µm	single slice	10.6GB
	h-j	LSM880	Leica 25x	0.95	1.33	2.5mm		0.10µmx0.10µm	2.5µm	single slice	120MB
S14	a-i	UM II -MVX10	Oly. 1X	0.25	1	65mm	0.63x	10.32µmx10.32µm	8µm	3D reconstruction	same data from Fig. 2b-d
S15	a-e	UM II -MVX10	Oly. 1X	0.25	1	65mm	1x	6.5µmx6.5µm	10µm	3D reconstruction	24GB
S16	a-c	UM II -MVX10	Oly. 2X	0.5	1.33/1.56	6mm	1.25x	2.6µmx2.6µm	4µm	3D reconstruction	39GB
S17	a	UM II	4X corr.	0.28	1.56	10mm		1.625µmx1.625µm	8µm	entire scan projection	57.8GB
	b-d	UM II	4X corr.	0.28	1.56	10mm		1.625µmx1.625µm	8µm	80µm thick projection	same data from Fig S17a
	e	UM II	4X corr.	0.29	1.57	10mm		1.625µmx1.625µm	8µm	80µm thick projection	42.1 GB
S18	a	UM II -MVX10	Oly. 2X	0.5	1.33/1.56	6mm	1x	3.25µmx3.25µm	8µm	1.6mm thick projection	same data from Fig. 5b
	b-d	UM II -MVX10	Oly. 2X	0.5	1.33/1.56	6mm	2x	1.625µmx1.625µm	10µm	(b)600µm, (c) 500µm, (d)400µm thick projections	same data from Fig. 5c-e
	e-g	UM II -MVX10	Oly. 2X	0.5	1.33/1.56	6mm	2x	1.625µmx1.625µm	6µm	1.6mm thick projection	61GB
S19	a,b	UM II	4X corr.	0.29	1.57	10mm		1.625µmx1.625µm	8µm	(a) 1.92mm, (b)640µm thick projections	474GB
	c-e	UM II -MVX10	Oly. 1X	0.25	1	65mm	2x	3.25µmx3.25µm	10µm	800 µm thick projections	103GB
	f-g	UM II -MVX10	Oly. 1X	0.25	1	65mm	3.2x	2µmx2µm	8µm	240µm thick projections	18GB
S20	a,b	LSM880	Zeiss 40X	1.3	1.518	0.21mm	1x	0.21µmx0.21µm	4µm	3D reconstruction	13GB
S21	a,d,g	UM II -MVX10	Oly. 2X	0.5	1.33/1.56	6mm	1.6x	2µmx2µm	6µm	3D reconstructions	(a)232GB, (d)114GB, (g)199GB
	b,e,h	UM II -MVX10	Oly. 2X	0.5	1.33/1.56	6mm	1.6x	2µmx2µm	6µm	30µm thick projections	(b)232GB, (e)114GB, (h)199GB
	c,f,i	UM II -MVX10	Oly. 2X	0.5	1.33/1.56	6mm	1.6x	2µmx2µm	6µm	single slices	(c)232GB, (f)114GB, (i)199GB
S22	a,b	UM II -MVX10	Oly. 2X	0.5	1.33/1.56	6mm	1.6x	2µmx2µm	6µm	3D reconstructions	18GB
	c,d	UM II -MVX10	Oly. 2X	0.5	1.33/1.56	6mm	1.6x	2µmx2µm	6µm	3D reconstructions	62GB
	e,f	UM II -MVX10	Oly. 2X	0.5	1.33/1.56	6mm	1.6x	2µmx2µm	6µm	3D reconstructions	73GB
	g	UM II -MVX10	Oly. 2X	0.5	1.33/1.56	6mm	1.6x	2µmx2µm	6µm	quantification on 3d reconstructions	3.35TB for 9 samples

Legend of abbreviations

Imaging Systems

UM II	LaVision BioTec - UltraMicroscope II
UM II -MVX10	LaVision BioTec - UltramicroscopeM II -MVX10
LSM880	Zeiss confocal LSM880 with Airyscan
AxioZoom	Zeiss AxioZoom EMS3/SyCoP3

NA	Numerical aperture
RI	Refractive Index
WD	Working distance
n.a.	not applicable

Objectives

Oly. 1X	Olympus MV PLAPO 1x/0.25 NA
Oly. 2X	Olympus MVPLAPO2XC
4X corr.	Olympus XLFLUOR4x corrected
Oly. 25X	Olympus XLPLN25X
Zeiss 20X	Zeiss Clr Plan-Neofluar 20x
Zeiss 40X	Zeiss ECPlan-NeoFluar 40x/1.30 Oil DIC M27
Leica 25X	Leica HCX IRAPO L 25x

Supplementary Table 2

Imaging specifications